Budding transitions of fluid-bilayer vesicles: The effect of area-difference elasticity

Ling Miao,* Udo Seifert,† Michael Wortis, and Hans-Günther Döbereiner‡

Physics Department, Simon Fraser University, Burnaby, British Columbia, Canada V5A 1S6

(Received 16 August 1993)

Budding and vesiculation are prominent shape transformations of fluid lipid-bilayer vesicles. We discuss these transitions within the context of a curvature model which contains two types of bending energy. In addition to the usual local curvature elasticity κ, we include the effect of a relative areal stretching of the two monolayers. This area-difference elasticity leads to an effective nonlocal curvature energy characterized by another parameter $\bar{\kappa}$. We argue that the two contributions to the curvature energy are typically comparable in magnitude. The model interpolates smoothly between the spontaneous-curvature model ($\bar{\kappa}=0$) and the bilayer-couple model ($\bar{\kappa} \rightarrow \infty$), discussed previously in the literature. Conceptually, this model is not new; however, neither its consequences nor its relation to experiment has previously been explored in detail. In particular, budding is discontinuous (first order) for small $\bar{\kappa}$ but changes via a tricritical point to continuous (second order) for large $\bar{\kappa}$. The order of the budding transition depends on both the ratio $\bar{\kappa}/\kappa$ (which is a material parameter) and the initial area difference between the inner and outer monolayers (which can be modified by appropriate treatment of the vesicle). Estimates suggest that, under typical laboratory conditions, the budding process should be discontinuous, in apparent disagreement with some recent experiments. Possible reasons for this discrepancy are discussed. We propose, in particular, that hysteretic effects are important and that the observed behavior may reflect a spinodal instability.

PACS number(s): 82.70.−y, 87.22.Bt, 68.15.+e, 68.60.Bs

I. INTRODUCTION

Fluid-phase phospholipid bilayers in an aqueous solution may form giant (10–20 μm) vesicles of single-sphere topology. Experiments have shown that these vesicles display a rich variety of shapes, as external conditions (temperature, osmotic pressure, etc.) are varied [1–9]. As these parameters change, vesicles undergo distinct transformations from one class of shapes to another. In this paper we focus particularly on the shape transformations called "budding" and "vesiculation."

The term "budding" is often used loosely to describe the multistep process in which a single spherical (or prolate) parent vesicle undergoes a sequence of shape changes resulting in the formation of a distinct daughter vesicle still linked to the parent via a narrow neck. We shall in what follows restrict "budding" to refer to the distinct transition at which up-down symmetry is broken and the vesicle passes from a symmetric prolate or dumbbell shape to a pear shape, without reflection symmetry. "Vesiculation," on the other hand, distinguishes the (singular) limit at which the radius of the neck connecting the mother and the daughter vesicles becomes microscopic.

Our present understanding of the diversity of vesicle shapes and of the transformations occurring between distinct shapes has largely been based on two simple models. In the spontaneous-curvature (SC) model, originally proposed by Canham [10] and Helfrich [11], a fluid lipid-bilayer vesicle is modeled by the energy functional [12]

$$E[C_1, C_2] \equiv \frac{\kappa}{2} \oint dA \, [C_1(\mathbf{r}) + C_2(\mathbf{r}) - \bar{C}_0]^2 \, . \qquad (1)$$

In this expression, $C_1(\mathbf{r})$ and $C_2(\mathbf{r})$ are the principal curvatures at the point $\mathbf{r}$ of the membrane surface, and $\bar{C}_0$, called the spontaneous curvature, is a parameter reflecting possible asymmetry between the two leaves of the bilayer. The integral is over the entire surface and is dimensionless, so the bending elastic constant κ sets the energy scale.

A different model—the bilayer-couple or ΔA model, based on the so-called bilayer-couple hypothesis [13] and closely related work of Evans [14] and Helfrich [15]—was first explored systematically by Svetina, Žekš, and co-workers [16–18]. Here, it is assumed that the area per lipid molecule is fixed and that there is no molecular exchange between the two leaves. Thus the areas of the individual leaves remain fixed. Under the condition that the two leaves are everywhere separated by the same spacing D with $D \ll R$ (the overall vesicle size, approximately 10–20 μm), ΔA is related to the local curvature by

$$\Delta A = D \oint dA \, (C_1 + C_2) \, , \qquad (2)$$

which is correct to order D/R. In energy minimization, the condition (2) becomes a constraint on the integrated mean curvature of allowed shapes. The energy functional

in this model,

$$G[C_1,C_2] \equiv \frac{\kappa}{2} \oint dA (C_1+C_2)^2 , \qquad (3)$$

is the same as Eq. (1) except that the spontaneous curvature $\bar{C}_0$ has been set to zero [19].

For phospholipid bilayers, it turns out that the bending rigidity κ is large on the scale of thermal energies at room temperature. Thus thermal fluctuations can be neglected, and the equilibrium configuration predicted by each model is just the shape which minimizes the bending energy subject to the appropriate constraints. Since the energy scale associated with a macroscopic stretching of the bilayer is several orders of magnitude higher than that involved in bilayer bending [4,20], the surface area of a vesicle is effectively constant under bending deformation. The volume enclosed by a vesicle is kept fixed in experiments by controlling the interior and exterior osmolarity. Thus both models obey constraints of fixed surface area and volume, while the ΔA model requires fixed area difference as a third constraint. In fact, the two models are related by a Legendre transformation [18].

In their pioneering work on the SC model, Deuling and Helfrich [21] found a catalog of possible axisymmetric vesicle shapes. Among those shapes were prolate and oblate ellipsoids, stomatocytes, and discocytes, some of which resembled the shapes of human red blood cells. The full systematics of these shapes and shape transformations has only been elucidated recently [22,23]. In particular, budding and vesiculation have now been studied in detail in both of the above models. Predictions of the two models for the character of the budding transition turn out to be strikingly different: The SC model predicts that the budding transition is discontinuous, whereas the ΔA model predicts that it is continuous, via pear-shaped intermediates. In both models the asymmetric shapes finally evolve smoothly towards vesiculation.

In recent experiments [6–9], all the stationary shapes found in the theoretical calculations have, indeed, been seen [24]; however, the budding sequences seem to be more complex than those predicted by either of the two models [25]. In a typical experiment, the temperature of the system is slowly increased. Normal thermal expansion then leads to changes in the area and volume of the vesicles, thus inducing shape transformations. One can follow in this way a sequence of shape changes which starts from a spherical or nearly spherical initial shape and proceeds via a prolate ellipsoid to budding and full vesiculation. Experiments find two distinct scenarios: (a) The prolate ellipsoid undergoes a shape transition at which the up-down symmetry is continuously broken, resulting in a pear shape; subsequently, the pear undergoes a second now-discontinuous transition which produces two spheres connected by a narrow neck. (b) The (symmetric) prolate ellipsoid buds discontinuously, directly to a shape consisting of two spheres connected by a narrow neck.

The continuous budding of scenario (a) is consistent with the predictions of the ΔA model; the discontinuous budding of scenario (b) is consistent with the predictions

of the SC model. Neither model contains the discontinuous vesiculation observed in scenario (a). Furthermore, experimentally, different vesicles from the same preparation (i.e., the same lipid in the same aqueous solution) may be seen to follow different scenarios. Unfortunately, neither the SC nor the ΔA models allows such differentiation. In fact, it has been shown that pretreatment of a vesicle before observation can affect its transition sequence. For example, precooling a vesicle for several hours always induces outside budding, whereas vesicles without such treatment may show other sequences, such as a transition to a stomatocyte shape followed by inverse (i.e., inside) vesiculation [7].

Thus it would appear that both the SC and ΔA models contain essential elements of the physics of these bilayer systems; yet, neither is fully consistent with available experiments. The SC model attributes the tendency of the vesicle to bud outside or inside to some intrinsic asymmetry (presumably chemical in origin) belonging to the bilayer. If this were true, then all similarly prepared vesicles (e.g., all vesicles in a given batch or preparation) would behave in the same way. This is manifestly contrary to observation. The ΔA model explains the diversity of shapes in a given preparation on the basis of whatever (unknown) mechanisms fix—e.g., at closure—the numbers of lipid molecules in the inner and outer leaves of the bilayer. However, the ΔA model predicts that budding is always continuous, which is inconsistent with experiments. Thus we are motivated to search for a model which retains the flexibility of the ΔA model but allows first-order budding.

In this paper, we investigate a model in which the areas of the individual monolayers are not fixed (as they are in the ΔA model) but can expand elastically under tensile stress. In this scenario, each monolayer has a preferred or relaxed area (A_0^{in} or A_0^{out}), based strictly on the number of lipid molecules it contains, but can have an actual area (A^{in} or A^{out}) which may be larger or smaller, provided that an appropriate cost in elastic energy is paid. The effect of stretching was recognized early on by Helfrich [11] and Evans [14] and was studied later by Svetina, Brumen, and Žekš [17]. The stretching modulus K of phospholipid films is sufficiently large so that for flaccid (i.e., nonpressurized) vesicles the stretching due to curvature-induced pressure differences causes only a negligible departure of the overall area A from its relaxed value A_0. On the other hand, the effect of stretching on the already-small area difference, $\Delta A \equiv A^{out} - A^{in}$, is fractionally important. The overall result, worked out in Appendix A (see also Ref. [17]), is an elastic stretching energy associated with the difference ($\Delta A - \Delta A_0$). This inclusion leads to a model defined by the energy functional,

$$W \equiv \frac{\kappa}{2} \oint dA [C_1(\mathbf{r}) + C_2(\mathbf{r}) - C_0]^2$$

$$+ \frac{\bar{\kappa}}{2} \frac{\pi}{AD^2} (\Delta A - \Delta A_0)^2 , \qquad (4)$$

and subject to constraints on the enclosed volume V, the total surface area A, and the relaxed (initial) area

difference, $\Delta A_0 \equiv A_0^{\text{out}} - A_0^{\text{in}}$. This model will be referred to henceforth as the area-difference elasticity (ADE) model. The first term is just the bending energy of the SC model (1), only with the spontaneous curvature now designated by C_0 instead of $\bar{C}_0$ (for future notational convenience). The second term is the elastic area-difference stretching energy, as derived in Appendix A. Note that the ADE model reduces in two limits to the SC model ($\bar{\kappa} \to 0$) and the ΔA model ($\bar{\kappa} \to \infty$).

The new modulus, $\bar{\kappa}$, appearing in Eq. (4) has units of energy, so the ratio, $\alpha \equiv \bar{\kappa}/\kappa$, is dimensionless. Note that, by virtue of Eq. (2), the area-difference term effectively couples local curvatures, $C_1(\mathbf{r})$ and $C_2(\mathbf{r})$, at points distant from one another on the vesicle surface (of course, the physical origin of this term is the *local* elastic energy, and it is the fluidity of the membrane, which makes the monolayer densities separately uniform, which allows the elastic energy to be rewritten in this effective nonlocal form). For this reason $\bar{\kappa}$ is sometimes called a "nonlocal" bending rigidity. The calculation given in Appendix A demonstrates that $\bar{\kappa}$ is generically of the same order of magnitude, KD^2, as the usual bending modulus κ. This equivalence is not an accident but reflects the fact that bending any layer (monolayer or bilayer) of nonzero thickness expands one side and compresses the other and, so, requires expenditure of elastic stretching energy. On this basis, we may anticipate that the ratio α is of order unity. In fact, in Appendix A, we use experimental data for κ, K, and D for two common phospholipids to estimate α, obtaining results in a range between 1 and 2 [15,26]. The first direct measurement [27] of the nonlocal bending rigidity for mixed stearoyl-oleoyl-phosphatidylcholine (SOPC) and palmitoyl-oleoyl-phosphatidylserine (POPS) bilayers used the tether-formation technique and found $\alpha = 1.1$ with a large range of uncertainty (0.5–4). Thus the effects of local and nonlocal bending rigidities are expected to be comparable, and the two terms must be treated on the same footing.

A preliminary report of our results for the phase diagram of the ADE model has been given in [28]. The effect of the interplay of the two curvature energies on the budding transition has also been investigated in [26] for a particular choice of parameters.

The plan of the present paper follows. In Sec. II we describe how the stationary shapes of the ADE model can be obtained from those of the ΔA model by a simple mapping. This greatly facilitates our study, since it shows that, despite the apparent nonlocality, the ADE model has the same catalog of stationary shapes as the SC and ΔA models. In Sec. III we study the phase diagram of the ADE model at zero spontaneous curvature. We find that for finite but nonzero α both first- and second-order budding are possible. Indeed, it turns out that, for any one fixed value of α, several qualitatively distinct budding and vesiculation trajectories are in general possible. In Sec IV we show that generalization to include nonzero spontaneous curvature is straightforward. We also explore in detail how the phase diagrams for the SC and ΔA models emerge as limiting cases of the ADE model. Section V is devoted to discussion of some typical calculated temperature trajectories, thus illustrating the important dependence of the predicted shapes on both the value of α and the initial area difference ΔA_0. Finally, in Sec. VI, we discuss the relation of these theoretical results to the available experiments. There is not yet complete agreement between the experiments and the equilibrium theory. We propose that the inclusion of hysteresis effects may resolve the outstanding discrepancies and we suggest further experiments to clarify this issue. Appendix A provides a microscopic derivation of the nonlocal bending energy. Details of phase-boundary calculations in the near-spherical limit are given in Appendix B.

II. STATIONARY SHAPES OF VESICLES: GENERAL REMARKS

The equilibrium shape of a vesicle is determined by minimizing the free energy (4) at fixed spontaneous curvature C_0 and relaxed monolayer area difference ΔA_0, subject to constraints of fixed volume V and surface area A. To incorporate the constraints, a variational free-energy functional of the form

$$\Phi[S] = W[S] + \Sigma A[S] + PV[S] \tag{5}$$

must be made stationary with respect to the degrees of freedom $[S]$ associated with the vesicle shape. Σ and P are Lagrange multipliers, which may be adjusted to attain the prescribed area and volume.

This nonlinear variational problem has, in general, several solutions, corresponding typically to shapes of distinct symmetry. Each individual shape evolves continuously as the parameters Σ and P are changed, thus producing a *branch* of mechanically equilibrated vesicle shapes. These stationary shapes may be minima or saddle points of the energy. To be observable, such a shape must be a (local) minimum. The lowest minimum provides the thermodynamic equilibrium configuration of the system, unless the true global minimum occurs at a boundary (as may be the case for fully vesiculated configurations [22, 29]).

Analysis is greatly facilitated by the fact that the ADE model and the ΔA model have exactly the same branches of stationary shapes. (A similar equivalence between the stationary branches of the ΔA and SC models has been noted earlier [18,23]). This correspondence is best seen as a mapping between the ADE model and the ΔA model, which we derive below. First, however, it is convenient to reduce the number of parameters by using the scale invariance of the bending energy. The ADE model has four different length scales R_A and R_V, defined by $A \equiv 4\pi R_A^2$ and $V \equiv (4\pi/3)R_V^3$, C_0^{-1}, and $\Delta A_0/D$. We choose to scale all distances with R_A, so we are left with three independent dimensionless variables: the reduced volume,

$$v \equiv \frac{V}{(4\pi/3)R_A^3} = \left[\frac{R_V}{R_A}\right]^3, \tag{6}$$

the reduced spontaneous curvature,

$$c_0 \equiv C_0 R_A, \tag{7}$$

and the reduced equilibrium area difference,

$$m_0 \equiv \Delta A_0 / (2DR_A) \equiv 4\pi \Delta a_0 . \qquad (8)$$

There are two energy parameters in the model, the usual bending elastic constant κ and the nonlocal bending constant $\bar{\kappa}$; however, only their dimensionless ratio, $\alpha = \bar{\kappa}/\kappa$, is relevant in the zero-temperature problem. Using these parameters, we rewrite the bending energy (4),

$$W(\alpha, v, c_0, m_0; [S]) = G(v, m; [S]) - 2c_0 m$$

$$+ 2\pi c_0^2 + \frac{\alpha}{2}(m - m_0)^2 , \qquad (9)$$

where we shall set $\kappa = 1$ for the remainder of the paper. $G(v, m; [S])$ is the bending energy of the ΔA model, defined in Eq. (3), and

$$m \equiv \oint dA (C_1 + C_2)/(2R_A) \equiv \Delta A/(2DR_A) \equiv 4\pi \Delta a \quad (10)$$

is the reduced version of the area difference (2) between the two monolayers. Note for reference that, for a sphere, $v = 1$ and $m = 4\pi$.

The relation (9) holds for all shapes S, stationary or not. The search for stationary shapes of the bending energy W proceeds in two steps: (i) For given α, c_0, and m_0, varying W in (9) with respect to the shape S at fixed m and v leads to the stationary shapes of the ΔA model, since the last three terms of (9) are constants under these conditions. This proves that every stationary shape of the ADE model is also a stationary shape of the ΔA model. (ii) Varying the energy W with respect to m then leads to the relation

$$m_0^{(n)}(m) = m + (G^{(n)'} - 2c_0)/\alpha , \qquad (11)$$

where $G^{(n)'} \equiv \partial G/\partial m$ denotes the derivative of the bending energy in the ΔA model at fixed A and V along a branch of stationary shapes labeled by n. For each stationary shape $S^{(n)}$, Eq. (11) establishes a one-to-one mapping from (m, v) in the ΔA model to $(m_0^{(n)}, v)$ in the ADE model. Note that it follows from the Legendre-transform relation between the ΔA and the SC models that $G^{(n)'} = 2\bar{c}_0$, where $\bar{c}_0$ is the scaled spontaneous curvature, $\bar{c}_0 \equiv \bar{C}_0 R_A$, in the SC model (1) which makes this particular shape stationary.

We conclude this section with two caveats concerning the rigor and generality of this treatment of the ADE shape problem. First, this study, like previous work [22,23], concentrates exclusively on axisymmetric vesicle shapes. The instability of axisymmetric shapes with respect to nonaxisymmetric perturbations can be analyzed, but only via a somewhat different approach [30]. Secondly, we have not compared the energies of all possible axisymmetric shapes corresponding to local minima of the bending energy (4) [or (9)]. Instead, we have restricted attention entirely to those shapes that are likely candidates for the global energy minimum in the region where budding and vesiculation occur.

III. BUDDING AND VESICULATION AT SPONTANEOUS CURVATURE $C_0 = 0$

The systematics of shapes and shape transformations of the ADE model is best represented by a "phase dia-gram" in the space spanned by the four parameters, α, v, c_0, m_0. Such a phase diagram exhibits several single-phase regions separated by phase boundaries. Within a single-phase region, the shape evolves smoothly as control parameters (like v or m_0) are varied. By contrast, shape changes across phase boundaries are abrupt, frequently but not necessarily involving a symmetry change. At phase boundaries, the total bending energy is always continuous; however, its first derivatives with respect to the parameters may change either discontinuously (at a "first-order" transition) or continuously (at a "second-order" transition).

Budding and vesiculation transitions involve the behavior of two specific branches of vesicle shapes. The *symmetric branch* consists of axisymmetric shapes with mirror symmetry with respect to an equatorial plane. In practice, such shapes resemble a prolate ellipse or a dumbbell. Mirror symmetry is broken for the *asymmetric branch*, and the corresponding shapes are termed "pearlike" (with a wide neck) or "budded" (with a narrow neck). This branch terminates at the "fully vesiculated" shapes, wherein the neck radius has formally shrunk to zero. Of course, physically, there is always a short-distance cutoff, so the neck attains microscopic dimensions (comparable to the bilayer thickness) but its radius remains nonzero.

We first discuss the case where the spontaneous curvature c_0 is zero. This case deserves special attention, because vesicles formed by a perfectly symmetric lipid bilayer fall into this category. All generic features of the ADE-model behavior are already present. Generalization to $c_0 \neq 0$ is straightforward, as we shall show in Sec. IV.

A. The phase diagram at $\alpha = 4$: Discontinuous versus continuous budding

For $c_0 = 0$, the phase diagram is three dimensional. A typical, two-dimensional fixed-α section is illustrated in Fig. 1 for $\alpha = 4$.

Symmetric-branch shapes have the lowest energy below the curve consisting of the two parts C^{pear} and D^{pear}. The lower limit of this region is set by a transition (not shown in Fig. 1) either to a nonaxisymmetric ellipsoid or to an oblate shape, depending on the specific values of v and m_0 (and α). Since these transitions are unrelated to budding and vesiculation, they will not be discussed further. The line C^{pear} is a phase boundary at which the symmetric shapes first become locally unstable with respect to a deformation that breaks the mirror symmetry. "C" stands for "continuous" and denotes a second-order transition. Just above the phase boundary C^{pear}, symmetric shapes are locally unstable with respect to a deformation that breaks the mirror symmetry. At larger reduced volumes (to the right of the point T) the transition between the symmetric branch and the asymmetric branch becomes discontinuous (D) along the phase boundary D^{pear}. The dotted line M^{pro} marks the continuation of the local-instability line C^{pear} into the asymmetric phase, so that, in the region between D^{pear} and M^{pro}, the symmetric shape remains locally stable,
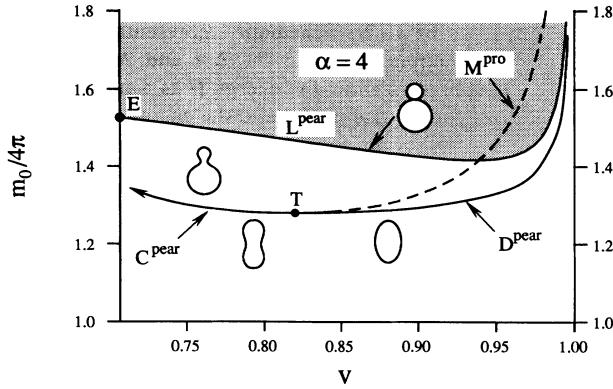
FIG. 1. Phase diagram in the (v, m_0) plane involving budding and vesiculation at fixed $\alpha = 4$. Symmetric and asymmetric shapes are separated by lines of continuous transitions, C^{pear}, or discontinuous transitions, D^{pear}. These lines of budding transitions meet at the tricritical point T. The line M^{pro} denotes the limit of metastability of the symmetric shapes. The line L^{pear} denotes the vesiculation line, where the neck size has shrunk to zero. It ends at the point E, where the limiting shape consists of two spheres of equal radii. In the shaded region above this line, multiplets involving several buds become relevant (see Ref. [22]).

even though it is not the lowest-energy shape. Thus M^{pro} is the limit of metastability (M) of the symmetric branch, which in thermodynamic language would be called a spinodal. The special point T, where C^{pear} and D^{pear} meet, we will call a "tricritical point." We denote its coordinates $(v_T(\alpha), m_{0,T}(\alpha))$. Finally, the line L^{pear} denotes the upper limit (L) of the asymmetric phase, where full vesiculation is attained. The neck radii of budded shapes go to zero continuously as L^{pear} is approached from below.

Such a phase diagram is constructed by using the mapping (11). In particular, the bending energy (9) of the ADE model for each branch of stationary shapes can be expressed as

$$W^{(n)}(\alpha, v, m_0(m)) = G^{(n)}(v, m) + \frac{\alpha}{2}[m - m_0(m)]^2 , \quad (12)$$

while its first and second derivatives are related to those of the bending energy $G^{(n)}(v, m)$ according to

$$\left. \frac{\partial W^{(n)}}{\partial m_0} \right|_{\alpha, v} = \left. \frac{\partial G^{(n)}}{\partial m} \right|_v \quad (13)$$

and

$$\left. \frac{\partial^2 W^{(n)}}{\partial m_0^2} \right|_{\alpha, v} = \frac{\alpha G^{(n)\prime\prime}(v, m)}{\alpha + G^{(n)\prime\prime}(v, m)} , \quad (14)$$

where

$$G^{(n)\prime\prime}(v, m) \equiv \left. \frac{\partial^2 G^{(n)}}{\partial m^2} \right|_v . \quad (15)$$

The structure of the mapping based on Eqs. (12)–(14) is illustrated in Fig. 2, which shows the energy G of the

ΔA model (as a function of m [23]) and the energy W of the ADE model (as a function of m_0) for both symmetric and asymmetric branches. At the bifurcation point C, the energy curves of the two branches have equal first derivatives. This property is preserved as m is mapped to m_0 [according to Eq. (11)] and $G^{(s,a)}(v, m)$ are transformed to $W^{(s,a)}(\alpha, v, m_0)$ by Eq. (12). Thus, in the neighborhood of the bifurcation point, the energy difference ΔW between the two branches in the ADE model can be expressed in terms of second derivatives of W,

$$\Delta W \equiv W^{(s)}(\alpha, v, m_0) - W^{(a)}(\alpha, v, m_0)$$
$$= \tfrac{1}{2}[W^{(s)\prime\prime}(\alpha, v, m_{0,C}) - W^{(a)\prime\prime}(\alpha, v, m_{0,C})]$$
$$\times (m_0 - m_{0,C})^2 . \quad (16)$$

Finally, these second derivatives of W can be obtained from corresponding second derivatives of G via Eq. (14), so the entire energetics of the ADE model in the vicinity of the bifurcation point, $m_{0,C} = m_C + G^{(s,a)\prime}(v, m_C)/\alpha$, can be related to properties of the ΔA model.

We have established numerically the following properties of the second derivatives of the bending energy $G^{(n)}(v, m)$ of the ΔA model in the interval $0.72 < v < 1$: (i) For the symmetric branch, $G^{(s)\prime\prime}(v, m)$ is positive for all values of m; (ii) for the asymmetric branch $G^{(a)\prime\prime}(v, m)$ is negative at the bifurcation point, increases monotonically, and reaches a positive value at the vesiculation point; and (iii) the magnitude of $G^{(a)\prime\prime\prime}(v, m_C)$ increases monotonically with v and eventually diverges in the limit $v \to 1$. Finally, it is useful to know the behavior of the mapping (11) near the bifurcation point: Differentiating with respect to m leads to the relation

$$\frac{\partial m_0^{(n)}}{\partial m} = 1 + \frac{1}{\alpha} G^{(n)\prime\prime}(v, m) , \quad (17)$$

which holds for both symmetric and asymmetric branches. It follows from Eq. (17) that $\partial m_0^{(s)}/\partial m$ is positive everywhere on the symmetric branch, while on the asymmetric branch $\partial m_0^{(a)}/\partial m$ is positive everywhere on the symmetric branch, while on the asymmetric branch $\partial m_0^{(a)}/\partial m$ changes sign at the point $v = v_T(\alpha)$, where $G^{(a)\prime\prime}(v, m_C) = -\alpha$.

These properties allow us to distinguish two different scenarios for bifurcation in the ADE model, corresponding to the continuous and discontinuous transitions, C^{pear} and D^{pear}, respectively.

(a) For $v < v_T(\alpha)$, the mapping (11) is monotonic for both the symmetric and asymmetric branches, and ΔW is positive, as follows from Eqs. (13)–(15). Therefore the topology of the energy diagram of the ΔA model is well preserved, as illustrated in Fig. 2(a), so the symmetry-breaking transition is continuous. The corresponding phase boundary C^{pear} is given as

$$m_{0,C}(\alpha, v) = m_C(v) + \frac{1}{\alpha} G^{(s,a)\prime}(v, m_C(v)) . \quad (18)$$

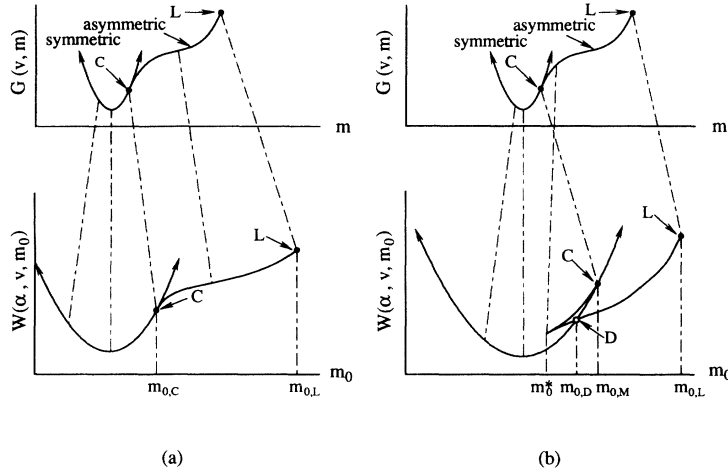(b) When $v > v_T(\alpha)$, the mapping (11) becomes non-monotonic for the asymmetric branch, while it remains

(a)   (b)

FIG. 2. Schematic representation of the mapping between the ΔA and ADE models. Figures show the energy G as a function of m for the ΔA model and the energy W as a function of m_0 for the ADE model. L denotes the vesiculated shape, where the neck size is zero, and C denotes the bifurcation point. For large α, as displayed in (a), the topology of the bifurcation is preserved in the ADE model and the budding transition is still continuous. For small α, as in (b), the symmetric branch develops a wing structure in the ADE model, thus rendering the budding transition discontinuous.

monotonic for the symmetric branch. In addition, for $m_0 \lesssim m_{0,C}$, $\Delta W < 0$. Thus the symmetric branch and the asymmetric branches interchange their relative positions. This change in topology leads to a "wing" structure in the energy diagram, as shown in Fig. 2(b). The position of the cusp on the left side of the wing is determined by $G^{(a)\prime\prime\prime}(v, m) = -\alpha$. An analogous wing structure occurs in the Landau theory of first-order transitions. The corresponding discontinuous budding transition occurs at D^{pear}, the precise location of which must be computed numerically. We performed such computations for $v < 0.90$. For larger values of the reduced volume v, numerical determination of the asymmetric branch becomes quite cumbersome; nevertheless, by representing these shapes using an expansion around the vesiculated limit (as described in Appendix E of Ref. [23]), one can obtain a good approximation to D^{pear}.

Related to the discontinuous transition is the issue of metastability. Both symmetric prolate (or dumbbell) and asymmetric pear (or narrow-necked) shapes are locally stable at the transition D^{pear}. Above D^{pear}, the symmetric shapes remain locally (meta)stable until they eventually develop a local instability with respect to asymmetric perturbation at the (spinodal) line M^{pro}, which is just the continuation of C^{pear} [Eq. (18)] beyond the tricritical point. Similarly, the asymmetric shape remains a local minimum of the bending energy below D^{pear}, only becoming locally unstable with respect to a perturbation which drives it to the symmetric shape when it reaches another spinodal line M^{pear} (not shown in Fig. 1). The location of the line M^{pear}, corresponding to the cusp in the wing structure of Fig. 2(b), is denoted m^*, and may be found by solving $G^{(a)\prime\prime\prime}(v, m^*) = -\alpha$. The tricritical point T at which C^{pear} and D^{pear} meet has coordinates $(v_T(\alpha), m_{0,T}(\alpha))$, where v_T satisfies the condition $G^{(a)\prime\prime\prime}(v_T, m_C) = -\alpha$ and $m_{0,T}$ is given through the mapping (11). This completes our discussion of the mathematical mechanism for budding transitions in the ADE model.

At the vesiculation boundary L^{pear}, equilibrium shapes consist of two spheres of different radii connected by an infinitesimal neck. Shapes in the pear region approach this limit smoothly. The form of this boundary may be

parametrized in terms of the area difference Δa (for $1 \leq \Delta a \leq \sqrt{2}$) by the two equations

$$v_L = 1 - \tfrac{3}{2}(\Delta a - 1)^2 - \tfrac{1}{2}(\Delta a - 1)^3 ,$$
$$m_{0,L} = 4\pi\Delta a + (4/\alpha)\Delta a/(\Delta a^2 - 1) . \tag{19}$$

We have not yet explored the interesting region beyond this limiting line. Presumably, there is some region where the fully vesiculated, two-sphere shapes persist. Beyond that, a prolate connected to a sphere and other multiply vesiculated shapes may also occur.

In the phase diagram, Fig. 1, and throughout this paper we have chosen somewhat arbitrarily to study reduced volumes $v > 0.72$. This locates us to the right of the special point $E(v = \sqrt{2}/2, m_0 = 4\sqrt{2}(\pi + 1/\alpha))$, where the vesiculation line L^{pear} ends in a vesiculated shape consisting of two spheres of equal radii. The point E is the right-hand limit of several domains of distinct minimum-energy shapes, so a detailed analysis of its neighborhood can be expected to be hard. For recent experiments, however, this point is unimportant, since observed vesiculations have typically involved a bud of considerably smaller size than the mother vesicle, corresponding to a reduced volume much closer to unity.

For reduced volume $v \lesssim 1$, all three of the boundaries L^{pear}, D^{pear}, and M^{pro} reach large values of the effective area difference m_0, as shown in Fig. 1. The leading terms as $v \to 1$ may be derived by developing in powers of $(1 - v)^{1/2}$ (see Appendix B). For L^{pear}, the phase boundary takes the form

$$m_0 = m_{0,L}(\alpha, v) = m_L(v) + (2/\alpha)\bar{c}_{0,L}(v) , \tag{20}$$

with $m_L(v) = 4\pi + O((1-v)^{1/2})$ and $\bar{c}_{0,L}(v) = \sqrt{3/2}(1-v)^{-1/2} + 3/2 + O((1-v)^{1/2})$. For D^{pear},

$$m_0 = m_{0,D}(\alpha, v) = (2/\alpha)\sqrt{3/2}(1-v)^{-1/2} + O(1) , \tag{21}$$

which is the same as Eq. (20) to leading order. It is more difficult to make exact statements about the spinodal line M^{pro}, however, we believe that the leading term is of the form $m_0 \sim (1-v)^{-1/2}$, only with a coefficient larger than that of Eqs. (20) and (21).

B. Dependence of the phase diagram on the parameter α: The SC and ΔA models as limiting cases

We describe in this subsection the complete phase diagram for budding and vesiculation in the ADE model, including dependence on the parameter α, which measures the relative strengths of the local and nonlocal bending rigidities. Figure 3 shows three sections, corresponding to different values of α, for which the calculations described in the preceding subsection were repeated. We discuss separately the cases (i) $\alpha < 4$ and (ii) $\alpha > 4$.

(i) As α decreases, the tricritical point moves monotonically towards smaller values of the reduced volume v. At $\alpha \simeq 1.2$, v_T reaches the value 0.72, so the point T has moved into the complicated region near the special point E, where several branches are in close competition for the lowest-energy shape. This region has not yet been explored in detail; however, it is clear that for $\alpha < 1.2$ the budding transition is exclusively discontinuous for $0.72 < v < 1$. When $\alpha = 0$, the results reported in Ref. [23] for the SC model with $C_0 = 0$ are recovered. As $\alpha \to 0$, the boundaries L^{pear} and L^{pear} move toward infinite values of m_0 as

$$m_{0,L}(\alpha,v) = 2\bar{c}_{0,L}(v)/\alpha + O(\alpha^0) \tag{22}$$

and

$$m_{0,D}(\alpha,v) = 2\bar{c}_{0,D}(v)/\alpha + O(\alpha^0) , \tag{23}$$

where $\bar{c}_{0,L}(v)$ and $\bar{c}_{0,D}(v)$ are the values of the reduced spontaneous curvature of the SC model at the boundaries L^{pear} and D^{pear}, respectively. Note that, as $\alpha \to 0$, L^{pear} and D^{pear} go to large values of m_0, which is consistent with the known fact [23] that, for the SC model with $\bar{C}_0 = 0$ in the regime $v > 0.72$, the equilibrium shapes are only prolates (dumbbells), and pears do not occur.

(ii) As the value of α increases from $\alpha = 4$, the tricritical point moves towards $v = 1$, and the budding transition becomes continuous for an increasing fraction of the range $0.72 < v < 1$. As $\alpha \to \infty$, the budding and the vesiculation phase boundaries both approach those of the ΔA model, as expected and in accordance with Eqs. (18) and (20). This limit can be explored in detail for v near one. For the vesiculation boundary L^{pear},

$$m_{0,L}(\alpha,v) = [4\pi + 4\pi\sqrt{2/3}(1-v)^{1/2} + O(1-v)]$$
$$+ \frac{1}{\alpha(1-v)^{1/2}}[2\sqrt{3/2} + O((1-v)^{1/2})] . \tag{24}$$

Note that the double limit, $\alpha \to \infty$ and $v \to 1$, is singular: For fixed $v \lesssim 1$, $m_{0,L}$ approaches a finite value close to 4π, as $\alpha \to \infty$; while, for large fixed α, $m_{0,L}$ diverges as $(1-v)^{-1/2}$, when $v \to 1$. Similarly, for the continuous-budding boundary C^{pear},

$$m_{0,C}(\alpha,v) = [4\pi + O(1-v)]$$
$$+ \frac{1}{\alpha(1-v)^{1/2}}[\mathrm{const} + O((1-v)^{1/2})] , \tag{25}$$
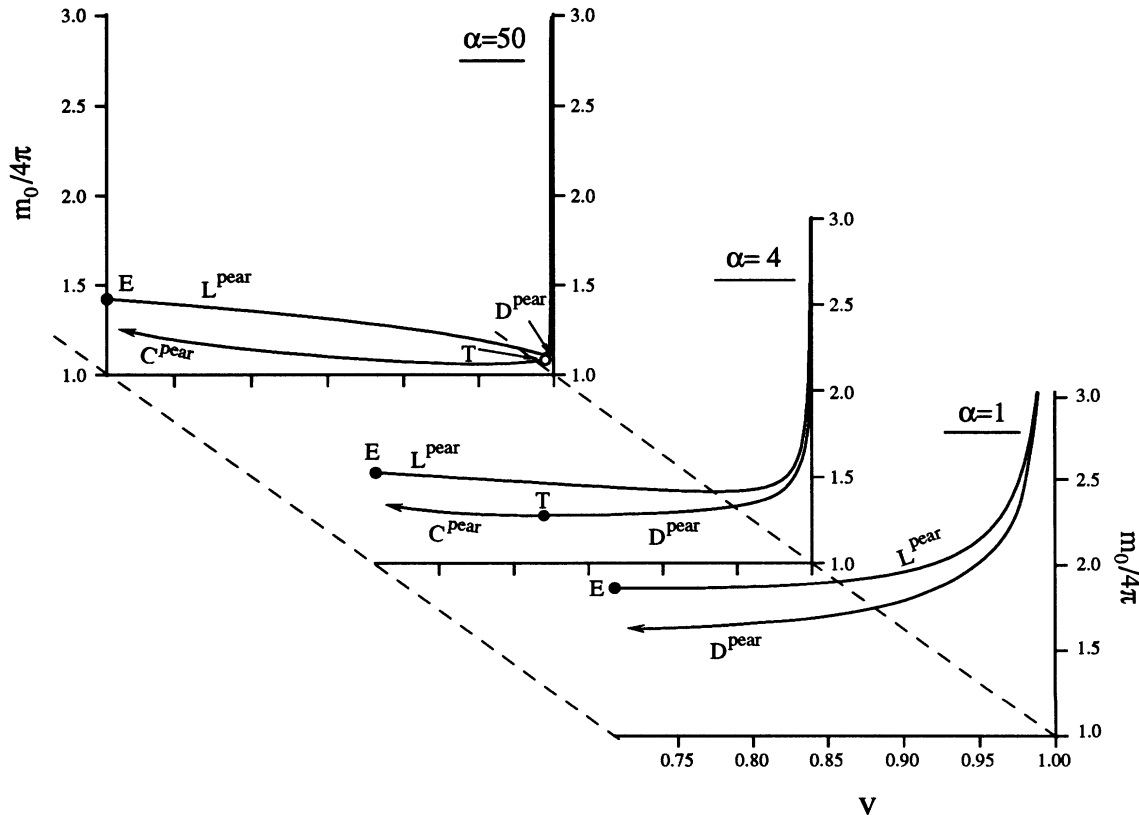

FIG. 3. Phase diagram for various values of α. For $\alpha = 1$, the budding transition is discontinuous (D^{pear}) over the range of reduced volume shown. For $\alpha = 50$, the budding is continuous (C^{pear}), except very close to $v = 1$ (we can only provide an upper bound (in v and m_0) to the tricritical point denoted by the open circle).

which ends at the tricritical point and is, again, singular in the double limit. We were not able to calculate rigorously the behavior of the tricritical point in the limit $\alpha \to \infty$. Our best guess is that $1-v_T(\alpha) \sim 1/\alpha$ and $m_{0,T}(\alpha) \sim 4\pi + 1/\sqrt{\alpha}$.

IV. BUDDING AND VESICULATION AT NONZERO SPONTANEOUS CURVATURE

Nonzero values of the spontaneous curvature C_0 result from the fact that a lipid bilayer may have a tendency to curve one way or the other, due, for example, either to intrinsic chemical asymmetry between the two leaves and/or to a chemical asymmetry between the adjacent (interior and exterior) aqueous environments [14]. Extension of the results of Sec. III to cover $C_0 \neq 0$ turns out to be technically straightforward. By defining the new variable,

$$\overline{m}_0 \equiv m_0 + 2c_0/\alpha , \qquad (26)$$

we can express the bending energy (9) as

$$W^{(n)}(\alpha, v, c_0, \overline{m}_0) = G^{(n)}(v, m) + \tfrac{1}{2}\alpha(\overline{m}_0 - m)^2$$
$$+ \left[2\pi + \frac{2}{\alpha}\right]c_0^2 - 2c_0\overline{m}_0 , \qquad (27)$$

where $\overline{m}_0$ and m are related by the mapping,

$$\overline{m}_0 = m + \frac{1}{\alpha}G^{(n)\prime}(v, m) . \qquad (28)$$

For a fixed nonzero c_0, the functional dependence of the bending energy $W^{(n)}$ on $\overline{m}_0$ differs from that for $c_0 = 0$ only by a constant plus a term linear in $\overline{m}_0$, as shown by Eq. (27). Neither term enters the second derivative of $W^{(n)}$. Thus our previous discussions both of the preservation of the topology of the energy curves by the mapping and of the location of the tricritical point continue to hold. In particular, for fixed c_0 and $v < v_T$, the location of the phase boundary C^{pear} is given by

$$m_{0,C}(c_0, v) = \overline{m}_{0,C}(v) - \frac{2c_0}{\alpha}$$
$$= m_C(v) + \frac{1}{\alpha}[G'(v, m_C) - 2c_0] . \qquad (29)$$

Similarly, for $v > v_T$, the discontinuous budding boundary D^{pear} is determined from the condition

$$W^{(s)}(\alpha, v, c_0, \overline{m}_0) = W^{(a)}(\alpha, v, c_0, \overline{m}_0) , \qquad (30)$$

which becomes

$$G^{(s)}(v, m^{(s)}(\overline{m}_0)) + \frac{\alpha}{2}[\overline{m}_0 - m^{(s)}(\overline{m}_0)]^2$$
$$= G^{(a)}(v, m^{(s)}(\overline{m}_0)) + \frac{\alpha}{2}[\overline{m}_0 - m^{(a)}(\overline{m}_0)]^2 . \qquad (31)$$

This condition is identical to the one for determining the C^{pear} when $C_0 = 0$, only with m_0 now replaced by $\overline{m}_0$. The solution is

$$\overline{m}_{0,D}(v) \equiv m_{0,D}(c_0, v) + 2c_0/\alpha = m_{0,D}(c_0 = 0, v) , \qquad (32)$$

where $(v, m_{0,D}(c_0 = 0, v))$ defines the discontinuous phase boundary in Fig. 1.

These results show that the fixed-α section of the budding phase diagram for a nonzero value of c_0 is identical to the $c_0 = 0$ phase diagram (Fig. 1) except for a shift of m_0 by $-(2/\alpha)c_0$.

The ADE model recovers the SC model and the ΔA model as its two limiting cases, $\alpha \to 0$ and $\alpha \to \infty$, just as it did for $C_0 = 0$. This feature is illustrated in Fig. 4, which shows a three-dimensional phase diagram for budding and vesiculation in the parameter space (α, c_0, m_0) for a typical (fixed) value of the reduced volume ($v = 0.8$). In the limit $\alpha \to \infty$, which corresponds to the ΔA model, the continuous symmetry-breaking transition C^{pear} and the final vesiculation L^{pear} are represented asymptotically by the two straight lines $m_0 = m_C(v)$ and $m_0 = m_L(v)$ [23], respectively, independently of c_0. As $\alpha \to 0$, the budding and vesiculation boundaries are, again, two straight lines, $c_0 = \overline{c}_{0,D}(v)$ and $c_0 = \overline{c}_{0,L}(v)$ [22,23], independently of m_0. The tricritical line

$$m_{0,T}(c_0, v) = m_C(v) + [G'_C(v) - 2c_0]/\alpha_T(v) ,$$
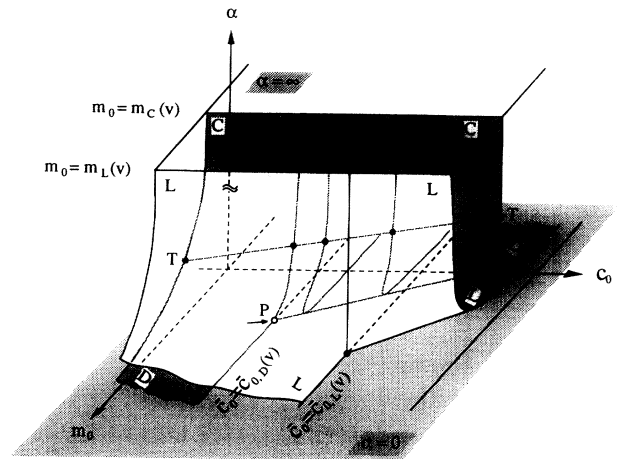$$\alpha_T = -G^{(a)\prime\prime}(v_C) , \qquad (33)$$

FIG. 4. Three-dimensional (α, c_0, m_0) phase diagram at a typical (constant) reduced volume. Two transition surfaces are shown. The rear (shaded) one corresponds to budding and the front (unshaded) one corresponds to vesiculation. As $\alpha \to \infty$ (one of the limiting cases), the two sheets asymptotically approach their limits, represented by the two lines $m_0(v) = m_C(v)$ and $m_0(v) = m_L(v)$, respectively. These limit lines are independent of C_0, as in the ΔA model; when $\alpha \to 0$, the discontinuous budding at $\overline{c}_{0,D}$ and the final vesiculation at $\overline{c}_{0,L}$ predicted by the SC model are asymptotically recovered. T denotes the tricritical line, which separates the continuous budding transitions, represented by the sheet C, from the discontinuous budding transitions, represented by the sheet D. The budding sheet splits along $c_{0,D} = \overline{c}_{0,D}$, and the two parts develop in opposite directions. The splitting terminates at the point P with coordinates $(\alpha = 0, c_0 = \overline{c}_{0,D}, m_0 = (m_{s,D} + m_{a,D})/2)$, where $m_{s,D}$ and $m_{a,D}$ are the actual area differences of the symmetric and asymmetric shapes at the first-order transition point in the SC model. The vesiculation sheet has a similar topology, with a splitting along the line $c_0 = \overline{c}_{0,L}$. Its splitting terminates at $(\alpha = 0, c_0 = \overline{c}_{0,L}, m_0 = m_L)$.

separates the continuous bifurcations (the sheet C) from the discontinuous budding (the sheet D). The asymptotic limits of each of these two sheets, as $\alpha \to \infty$ and $\alpha \to 0$, are two mutually perpendicular straight lines. The twisting of the sheets C and D, and the splitting of the sheet D along the line $c_0 = \bar{c}_{0,D}(v)$ may be regarded simply as consequences of the geometry imposed by these two limiting cases.

V. TEMPERATURE TRAJECTORIES

Most (but not all) experiments on vesicle shapes involve systematic observation of temperature-driven shape transformations. Thus, in preparation for discussion of experimental observations in the final section, it is important to establish [23] (a) how the model parameters, $A, V, \Delta A, \alpha$, and C_0, may be expected to vary with temperature and (b) how the trajectories through parameter space defined by $v(T)$, $m_0(T)$, etc., intersect the boundaries of the phase diagrams developed in the last two sections.

Temperature increase leads to thermal expansion of both the membrane area A and the volume V of the enclosed aqueous interior. We focus on the simple case where the inner and outer monolayers of the bilayer are identical in composition and environment, so their thermal expansivities are the same [31],

$$\beta_A \equiv \frac{1}{A_0^{\text{out}}} \frac{dA_0^{\text{out}}}{dT} \equiv \frac{1}{A_0^{\text{in}}} \frac{dA_0^{\text{in}}}{dT} = \frac{1}{A_0} \frac{dA_0}{dT} \ . \tag{34}$$

The volume expansivity of the enclosed fluid (principally water) is appreciably smaller than the membrane area expansivity. Typical values are $\beta_V \simeq 3 \times 10^{-4}/\text{K}$, while $\beta_A \simeq 4 \times 10^{-3}/K$ for SOPC and dimyristoyl-phosphatidylcholine (DMPC) [20]. Thus, neglecting the volume expansion, one obtains the temperature variation of the reduced volume v,

$$\frac{dv}{dT} = -(3\beta_A/2)v \ . \tag{35}$$

The behavior $m_0(T)$ depends on the thermal response of both the membrane area and the bilayer thickness D. The temperature dependence of D has been measured for several phospholipids, including palmitoyl-oleoyl-phosphatidylcholine (POPC) and DMPC, by using NMR [32,33]. In their fluid ("liquid-crystalline") state, these phospholipid bilayers exhibit a decrease in thickness as temperature is increased, presumably due to entropic contributions of the molecular tails, so the thermal expansivity

$$\beta_D \equiv \frac{1}{D} \frac{dD}{dT} \tag{36}$$

is negative. In fact, for a number of lipids, the volume of a bilayer membrane in the fluid state has been shown to change by only about 0.07% per degree [33,34] and can, therefore, be considered effectively as constant over the temperature range explored in experiments. Thus $\beta_D = -\beta_A$ should be a good approximation, if it is assumed that $V_{\text{bilayer}} \simeq AD$. Under these assumptions, then, we infer a simple temperature dependence for m_0,

$$\frac{dm_0}{dT} = (\beta_A/2 - \beta_D)m_0 = (3\beta_A/2)m_0 \ . \tag{37}$$

Eliminating T, we find a simple relation between v and m_0,

$$m_0(T) = m_0(T_0) \frac{v(T_0)}{v(T)} \equiv \frac{\hat{m}_0}{v(T)} \ . \tag{38}$$

Temperature trajectories in the (m_0, v) plane can thus be parametrized by the reduced equilibrium area difference $\hat{m}_0$ for the corresponding spherical shapes. For the sake of simplicity, we shall assume that α is temperature independent (there is, as far as we know, no information available on temperature dependence of this parameter). Finally, for a first analysis, we shall assume $C_0 = 0$. Under these conditions, Eq. (38) completely specifies the temperature trajectories.

It will be useful in what follows to refer to the two specific trajectories which pass through the points T $(v_T(\alpha), m_{0,T}(\alpha))$ and E $(\sqrt{2}/2, \sqrt{2}(4\pi + 4/\alpha))$ (see Fig. 6). The corresponding initial values of $\hat{m}_0$ are

$$\hat{m}_{0,T} \equiv m_{0,T}(\alpha)v_T(\alpha) \ ,$$
$$\hat{m}_{0,E} \equiv 4\pi + 4/\alpha \ . \tag{39}$$

Figure 5 shows how the values of $\hat{m}_{0,T}$ and $\hat{m}_{0,E}$ depend on α. Note that these curves cross.

The special trajectories T and E divide the phase plane (v, m_0) into regions of distinct budding and vesiculation behavior. The relative positions of these special trajectories define three different regimes.

(A) For intermediate values of α, both trajectories T and E exist and $\hat{m}_{0,T} < \hat{m}_{0,E}$, as illustrated in Fig. 5. Within this framework, different initial area differences $\hat{m}_0$ lead to different characteristic thermally induced budding sequences (see Fig. 6).

(i) Discontinuous budding with vesiculation. For $\hat{m}_0 > \hat{m}_{0,E}$, increasing temperature causes the vesicle to follow a trajectory that crosses the discontinuous budding transition and leads to smooth vesiculation. Note, however, that the elliptical branch remains locally stable at the discontinuous phase boundary D^{pear} and does not develop local instability until reaching the spinodal line M^{pro}. Between D^{pear} and M^{pro} lies a region of metastability-hysteresis. Thus, upon slow heating, a prolate ellipse is expected to pass smoothly through the first-order boundary D^{pear} and to become unstable only just before M^{pro}, when the metastability barrier has decreased in height to $O(k_B T)$, so thermal fluctuations can drive the shape over the barrier to some new, lower minimum of the free energy. For large values of $\hat{m}_0$, the region of prolate metastability can extend well beyond the vesiculation line L^{pear}, so the new minimum may well be a fully vesiculated shape. In this way, it is possible that increasing-temperature trajectories in this regime may miss entirely the region of stable pears (see Sec. VI). Of course, M^{pro} eventually reaches the tricritical point, so, for smaller values of $\hat{m}_0$, the spinodal is still in the pear region. In general, the larger $\hat{m}_0$, the smaller is the temperature interval between D^{pear} and L^{pear}, the smaller
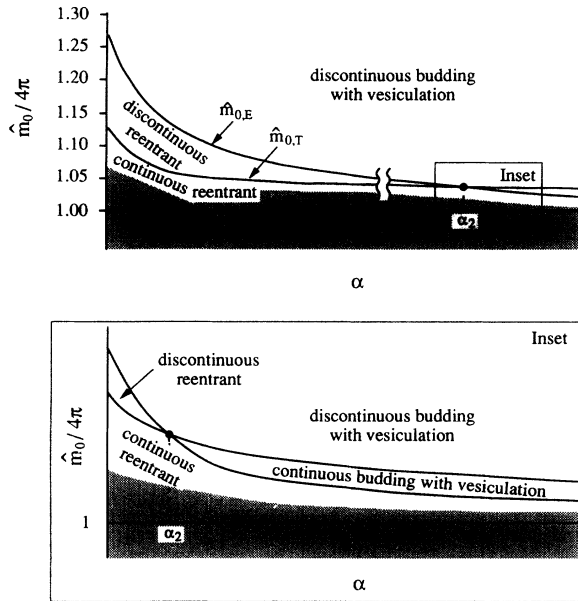
FIG. 5. Budding as a function of the equilibrium area difference $\hat{m}_0$ and α. For $\alpha > 6.5$ the curve $\hat{m}_{0,T}$ can no longer be obtained numerically. The schematic representation for large α (inset) shows the small region where continuous budding transitions with subsequent vesiculation exists. The gray area shows schematically the region in which the transition from prolates to pears is no longer present.

is the size of the vesiculated bud, and the more likely is hysteresis large enough to miss the pear.

(ii) Discontinuous budding without vesiculation. For $\hat{m}_{0,T} < \hat{m}_0 < \hat{m}_{0,E}$, the spherical vesicle, upon heating, undergoes discontinuous symmetry breaking; however, upon further increase of temperature, the vesicle will either become symmetric again *(discontinous reentrant trajectory)* and/or it will approach another limiting shape for $v < \sqrt{2}/2$ [35]. Since we have not analyzed shapes for $v < \sqrt{2}/2$, we cannot yet decide between these alternatives.

(iii) Continuous budding without vesiculation. For $\hat{m}_0 < \hat{m}_{0,T}$, the vesicle undergoes continuous symmetry breaking, as it passes into the pear region. Beyond this, it

may become symmetric again *(continuous reentrant trajectory)* or it may approach another limiting shape for $v < \sqrt{2}/2$. We have not determined the lowest value of $\hat{m}_0$ for which this trajectory occurs. For even lower values of $\hat{m}_0$, the trajectories miss the pear region entirely and may reach nonaxisymmetric or oblate and stomatocyte shapes.

The picture just described holds for intermediate values of α, $\alpha_1 < \alpha < \alpha_2$. The lower bound, $\alpha_1 \simeq 1.2$, of this regime is set somewhat arbitrarily at $v_T(\alpha_1) = 0.72$ (see Sec. III A). Numerical determination of the upper limit α_2, defined by $\hat{m}_{0,T}(\alpha_2) = \hat{m}_{0,E}(\alpha_2)$ (see Fig. 5), is quite difficult. We were able numerically to follow the tricritical point up to $\alpha = 6.5$, which is still in the intermediate regime. For large α, the asymptotic analysis of Appendix B shows that $\hat{m}_{0,E} < \hat{m}_{0,T}$. Thus we can conclude $6.5 < \alpha_2 < \infty$, but we do not know how tight this lower bound is. When $\alpha > \alpha_2$ or $\alpha < \alpha_1$, the characteristic budding scenarios are different from those described above.

(B) For large values of $\alpha (\alpha > \alpha_2)$ both T and E trajectories persist, but now reversed in order from regime (A). Again, there are three scenarios for thermally driven shape evolution.

(i) Discontinuous budding with vesiculation still occurs for $\hat{m}_0 > \hat{m}_{0,T}$. The discussion of metastability-hysteresis parallels that given for regime (A), scenario (i).

(ii) Continuous budding with vesiculation now becomes possible for $\hat{m}_{0,E} < \hat{m}_0 < \hat{m}_{0,T}$ as a result of the change of ordering of the T and E trajectories. Note, however, that the window in $\hat{m}_0$ for this to happen is very narrow, since the separation between $\hat{m}_{0,E}$ and $\hat{m}_{0,T}$ is small. Thus, to see this behavior, a delicate tuning of the initial area difference would appear to be necessary.

(iii) Continuous budding without vesiculation remains a possibility for $\hat{m}_0 < \hat{m}_{0,E}$. Upon heating, the vesicle follows a reentrant sequence, in which up-down symmetry is first broken in passing the continuous boundary C^{pear} and then restored, as this boundary is crossed again. In fact, there exists a smallest value of $\hat{m}_0$, below which the budding associated with prolate ellipses and pears is no longer present (as shown by the shaded region in Fig. 5). We have not calculated this value as a function of α.

(C) For small values of $\alpha (\alpha < \alpha_1)$, the situation is less
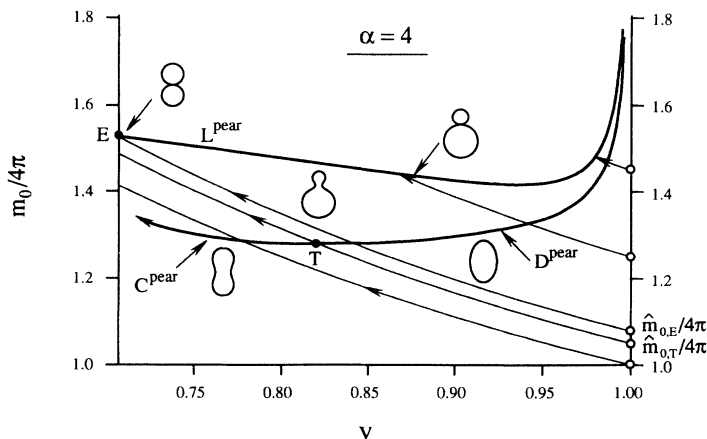

FIG. 6. Temperature trajectories in the (v, m_0) plane for $\alpha = 4$. All trajectories are represented as thin lines, with arrows pointing out the direction of a temperature increase, starting from a spherical shape but with different initial area differences $\hat{m}_0$. For large $\hat{m}_0$, one obtains discontinuous budding with vesiculation; for a small intermediate range of $\hat{m}_0$, discontinuous budding without vesiculation; and, for even smaller $\hat{m}_0$, continuous budding with reentrant behavior. The larger $\hat{m}_0$, the smaller the vesiculated bud at the limit line L^{pear}.

clear, since the evolution of the tricritical point with α has not yet been systematically investigated. For $\hat{m}_0 > \hat{m}_{0,E}$, there is discontinuous budding followed by vesiculation, and, since the transition to the pear region is first order, we expect hysteresis. For values of $\hat{m}_0$ near to but below $\hat{m}_{0,E}$, we expect a reentrant trajectory, in which the transitions into and subsequently out of the pear region are discontinuous.

In summary, the ADE model exhibits a variety of different temperature trajectories (even for a fixed value of α), depending on the equilibrium area difference $\hat{m}_0$. In particular, continuous budding with subsequent vesiculation occurs only in a restricted range of α and, even there, over a very narrow range of $\hat{m}_0$. These results were obtained under the assumption of zero spontaneous curvature. Analogous results for nonzero C_0 would require knowledge of the temperature dependence of C_0, for which there are so far no measurements available. Assuming C_0 to be temperature independent, one obtains the same scenarios for budding and vesiculation as discussed above, since nonzero C_0 just shifts the scale on the m_0 axis. In particular, the presence of a nonzero spontaneous curvature does not alter the value of α_1 below which all budding transitions are discontinuous.

VI. COMPARISON TO EXPERIMENTS

We close with a few comments on the relation between the predictions of the ADE model and the available experimental observations. It is convenient to structure these remarks in the form of questions and answers.

A. Can the budding and vesiculation scenarios described in Sec. I be explained by the ADE model?

Experiments [6–9] apparently see both continuous and discontinuous budding transitions, followed by vesiculation [see Sec. I, scenarios (a) and (b)]. Neither the SC nor the ΔA model can explain this diversity, since each of them contains one type of transition but not the other. As we have seen, the ADE model does allow both continuous and discontinuous budding, depending on the value of α (and, with some lesser significance, C_0). It even allows continuous and discontinuous transitions for a single value of α, provided the initial area difference m_0 is adjusted appropriately. In this sense, the ADE model is at least qualitatively successful.

On the other hand, closer examination reveals difficulties. To make a quantitative comparison with the experiments we need to know what value of $\alpha = \bar{\kappa}/\kappa$ to use. In Appendix A, we estimate this ratio as of order unity for common phospholipids ($\alpha \approx 1.1$ for DMPC and $\alpha \approx 1.4$ for SOPC). The only direct measurement of α that we are aware of is for SOPC+POPS mixed-lipid bilayers and used a tether-pulling technique [27]. This measurement gives $\alpha \approx 1.1^{+1.6}_{-0.8}$ consistent with our expectation but with a large uncertainty. These values of α are substantially smaller than α_2, so the theory predicts that any temperature-induced budding should be discontinuous. Note that this prediction is independent of both the initial area difference m_0 (see Fig. 3) and the value of the

spontaneous curvature. Such discontinuous budding [scenario (b)] has, indeed, been observed [8]. But, within this context, continuous symmetry breaking followed by a discontinuous shrinkage of the pear neck [scenario (a)] [7] cannot be explained by the ADE model. Not only is the continuous symmetry-breaking transition not possible for this low value of α but, in addition, the discontinuous transition from weak pears to strong pears or to a vesiculated phase is not available in the ADE model for any value of α.

B. Is there a possible explanation for the inconsistency between the predictions of the ADE model with $\alpha \approx 1$ and scenario (a)?

It is not clear at this writing whether this disagreement for budding scenario (a) is serious or whether it is an experimental artifact. One possibility provides a fairly straightforward explanation of the continuous symmetry breaking: It is not always easy to distinguish between unilamellar and multilamellar vesicles in the laboratory. The reason for this difficulty is that observations are done by light microscopy and, even with sophisticated techniques, it is impossible to resolve distances less than a few tenths of micron. Thus many determinations of membrane thickness are inferential and depend on looking for regions of lamellar separation, differences between the behavior of different vesicles from the same preparation, etc. If multilamellar vesicles are present, then these vesicles would have a larger effective value of α [36]. For a bilamellar vesicle, for example, treating both bilayers as elastic fluid sheets (as in Appendix A) leads to an effective $\alpha_{\text{eff}} = \alpha(D_{\text{bilayer}}/D)^2$, where α is the single-bilayer value and D_{bilayer} is the interbilayer distance. Suppose $D_{\text{bilayer}} = 2D + D_{\text{fluid}}$, where D_{fluid} is the thickness of any water layer separating the two bilayers. If $D_{\text{fluid}} = 0$, the enhancement of α is a factor of 4. For $D_{\text{fluid}} > 0$, it could be appreciably larger. For $\alpha > \alpha_2$, there is a range of initial area difference for which continuous budding followed by smooth vesiculation can occur. But, the discontinuous transition observed in scenario (a) between a weak pear and a narrow-necked or fully vesiculated shape still remains unexplained, without some additional mechanism [37].

Another possible explanation is that the shapes identified in scenario (a) as stable weak pears are, in fact, slow fluctuations and/or unstable dynamical intermediates. Experimentally, the issue centers on how to distinguish between continuous and discontinuous shape transitions. In practice, the experiments are done [7,8] by slowly ramping up [38] the temperature, while watching the shape evolution via video microscopy. In the early days temperature ramping rates of 0.3 °C/min were commonly used. More recently, DMPC experiments have been done with rates of 0.1 °C/15 min [7]. Ordinarily, shape equilibration after a temperature change takes only a few seconds and fluctuations are weak. Near the transition, however, strong shape fluctuations have been observed, sometimes lasting for periods of several minutes or more [39], so there are clearly some long time scales in the system. Furthermore, the observed shape must, of

course, evolve smoothly, as it passes through a transition, whether the transition be first order or second. Thus, even for discontinuous transitions, weak pears will be observed as dynamical transients.

These issues have not yet been adequately explored; however, the crucial questions are, what is responsible for the long time scales and can a fluctuating equilibrium shape be distinguished from a slow dynamical transient? One interpretation of the observations is that the transitions are continuous and that the long time scale is the usual critical slowing down characteristic of a second-order transition. Another interpretation, which we shall now explore, is that the long time scale is associated with approach to the spinodal line (M^{pro}) and that the observed weak pears are fluctuations and/or dynamical transients. From this perspective, the apparent extended region of weak pears is, in fact, a region of metastable prolate ellipses in which there are long-lived thermally induced pear fluctuations. In this interpretation, the observed discontinuous transition to a narrow-necked or fully vesiculated state is just the termination of metastability marginally before the spinodal M^{pro}, as a thermal fluctuation finally drives the system over the (small) remaining free-energy barrier and it falls to a new low-energy stable equilibrium.

There is some experimental evidence to support this interpretation. In the experiments [40] on DMPC, unexplained fluctuations of the "stable" pears back to the prolate ellipse were occasionally observed. Furthermore, in recent experiments on SOPC and DMPC [39] pear fluctuations lasting longer than 1 min are regularly observed [41].

To explore the plausibility of this interpretation, we must understand the characteristic time scales of the system. If the transition is first order (i.e., hysteretic), there are at least two time scales involved: The (locally) stable symmetric shape is, of course, subject to asymmetric (pearlike) fluctuations. These fluctuations are normally overdamped by the viscosity of the surrounding fluid, and they have a characteristic relaxation time which we shall call τ_1. Another scale, which we shall call τ_2, is the characteristic time for giant fluctuations, which carry the system over the kinetic barrier to a new minimum. When the height of the barrier is large compared to the thermal energy, these two scales are distinct, with $\tau_1 \ll \tau_2$.

A crude estimate of τ_1 can be obtained as follows: Consider a shape fluctuation which drives the symmetric prolate towards a pear. If the amplitude of this mode is a (measured in units of R), then the restoring force for such a fluctuation is $(\delta^2 W/\delta a^2)a$, which involves the second variation of the bending energy in the direction of this mode. At the instability, $v = v_c$, this quantity changes sign. Therefore $\delta^2 W/\delta a^2 \simeq c_1 \kappa(v - v_c)$, with a numerical coefficient c_1 which may be determined by diagonalizing the second variations. The coupling of the membrane to the surrounding liquid leads to a frictional force which has to balance the restoring force for such an overdamped motion. The frictional force is given by $c_2(\partial_t a)\eta R^3$, which follows from dimensional analysis, where $\eta \simeq 10^{-2} \mathrm{erg\, sec/cm^3}$ is the viscosity of water and c_2 is another numerical coefficient. Taking $(\partial_t a)\approx a/\tau_1$,

we find the time scale

$$\tau_1 = (c_2/c_1)\eta R^3/[\kappa(v_c - v)] . \tag{40}$$

For typical experimental values, $R \simeq 10 \,\mu\mathrm{m}$ for the size of the vesicle and $\kappa = 10^{-12}$ erg for the bending ridigity, we obtain $\tau_1 \simeq (10 \mathrm{\,sec})[(c_2/c_1)/(v_C - v)]$. Thus, far from the instability [i.e., for $(v_c - v)=O(1)$], we expect a time scale of several seconds for these long-wavelength shape fluctuations, which is consistent with typical observed times for achieving mechanical equilibrium far from any shape transition. However, close to the spinodal point (and also, of course, close to any real second-order transition), τ_1 diverges due to the factor $(v_c - v)$ in the denominator.

The second time scale, τ_2, which corresponds to the mean lifetime of the metastable prolate, is given by an exponential $\tau_2 = \tau_1 e^{\Delta W/k_B T}$. Here, τ_1 is the typical "microscopic" time, which is the inverse of an "attempt frequency," and ΔW is the energy barrier between the (metastable) prolate and the saddle point. Assuming a Landau-type expansion,

$$W = \kappa[c_1(v_c - v)a^2/2 - c_3 a^4/4 + c_4 a^6/6] , \tag{41}$$

we estimate the energy barrier ΔW near the instability as $\Delta W = \kappa c_1^2(v_c - v)^2/4c_3$. The two time scales, τ_1 and τ_2, become comparable when $\Delta W = k_B T$, i.e., for $(v - v_c) = (2c_3^{1/2}/c_1)(k_B T/\kappa)^{1/2}$. Using this estimate in (40) and taking $k_B T = 4 \times 10^{-14}$ erg gives a relaxation time

$$\tau_1 \simeq (c_2/2c_3^{1/2})\eta R^3/(\kappa k_B T)^{1/2} \simeq 50(c_2/2c_3^{1/2}) \mathrm{\,sec} \tag{42}$$

at the transition. One would need to know all the numerical factors for a more precise quantitative calculation; however, it is clear that for pearlike fluctuations a relaxation time on the order of minutes is entirely plausible near the transition. Of course, when the transition occurs, the slow diffusive motion over the barrier produces pear shapes as dynamical transients.

In summary, pear shapes may show up both as slow, overdamped dynamical fluctuations and as dynamical transients of the metastable prolate shape, as it finally becomes unstable. The discrepancy between observed scenario (a) and the theory would be resolved, if such shapes have been mistaken for stable pears.

C. The ADE model relies on variation of the model parameter $\bar{m}_0$ (the reduced value of the initial relaxed area difference) to explain the diversity of shapes and thermal trajectories seen in experiment. Is the range of values of this parameter required to fit the experiments physically reasonable?

This area difference is set at the time the vesicle is formed. Subsequent to closure, it can only change by lipid flip-flop, a process which we have assumed to be slow. Vesicle closure takes place in the lab, as water is added to the dry lipid [25], by a mechanism which is not understood in detail. Nevertheless, some crude estimates can be made: If the two monolayers (inner and outer) are

identical in composition and if the inner and outer fluids are the same, then the area difference is just $\Delta A_0(T) \equiv (N^{\text{out}} - N^{\text{in}}) a_0(T)$, where $a_0(T)$ is the optimal (relaxed) area per molecule at temperature T, and N^{out} and N^{in} represent the numbers of lipid molecules in the outer and inner monolayers, respectively. For a relaxed spherical vesicle with a radius of 10 μm, a bilayer thickness of 3 nm, and a mean area per molecule of 0.6 nm^2, the average number of lipid molecules in each monolayer is $N^i \simeq 2 \times 10^9$, whereas the optimal difference in the number of molecules between the two monolayers (when both monolayers are unstretched) is $\Delta N \equiv N^{\text{out}} - N^{\text{in}} \simeq 10^6$. Of course, initial closure may take place in configurations other than spherical. The relaxed area difference goes generally as CRD, where C is a constant, R is a typical vesicle dimension, and D is the bilayer thickness. For the sphere, $C = 8\pi$ and $\Delta a_0 = 1$. Other closure geometries lead to values of the constant C which can differ from this by factors of order unity, so we expect Δa_0 of order unity with typical fluctuations of the same order. This is broadly consistent with the range of shapes observed experimentally [7,8]. Note that ΔN of order 10^6 is much larger than $\sqrt{N}$, so random fluctuations of equal-area monolayers cannot account for the required area difference.

D. We have already observed [7,8] that precooling a vesicle tends to induce outside budding (when the vesicle is rewarmed). Can this be understood in the context of the ADE model?

These experimental observations [7,8] relate to vesicles which are cooled so that their surface area shrinks and they become turgid spheres. Characteristically in this state, all observable shape fluctuations cease. This is consistent with a state of lateral tension in which the higher elastic-energy scale, KR^2 (see Appendix A), comes into play, and the interior pressure rises dramatically. The question, then, is, can we in some way link this increase of interior pressure to an increase in Δa_0, which would, in turn, explain the subsequent exterior budding? An intriguing suggestion of Boroske, Elwenspoek, and Helfrich [42] provides just such a link. Helfrich proposed in another context that the flow of water through a membrane may produce a parallel transport of lipid along the pressure gradient. Thus, in our context, the water flow caused by the pressure gradient would carry lipids from the inner to the outer monolayer, thereby increasing Δa_0 and favoring outside budding. How this "induced" flip-flop might work at a microscopic level is not clearly established. One possibility is a simple entrainment of the lipid by the water flow. Alternatively, the stressing of the membrane might cause the formation of microscopic pores, connecting the inner and outer leaves of the bilayer. Whatever the mechanism, Helfrich estimates that one lipid molecule is transported by flow for every 5×10^5 water molecules. Using this figure, we may estimate a rough rate for the induced flip-flop of 10^6 lipid molecules for each 10 °C of cooling beyond the unstressed sphere. As outlined in the preceding paragraph, this is just the right order of magnitude to produce a significant shape change favoring outside vesiculation of small buds (see Fig. 6).

E. The ADE model has some attractive features but also some drawbacks. What experiments might be crucial to establishing its viability?

First, it should be pointed out that no simultaneous measurements of material parameters and shapes (or shape trajectories) has yet been done. Thus it would be very useful to be able to measure κ and $\bar{\kappa}$ (e.g., by tether pulling [27]) for some vesicle (thus determining α) and then to observe shapes for the same vesicle as temperature is varied. This would allow a straightforward comparison of observed and predicted shapes, which has not so far been possible. Such a measurement for a variety of vesicles could also put to rest any doubts about whether observed vesicles are unilamellar or multilamellar.

The main outstanding qualitative difficulty with the ADE model is the fact that the equilibrium behavior of the model is inconsistent with the observed budding scenario (a) (Sec. I). To establish the correctness of the hysteretic interpretation of the observations proposed in Sec. VI B above, it will be necessary to study shape fluctuations in this regime under careful temperature control and over observation times long enough to distinguish slow fluctuations from thermal drifts and dynamical transients. Experiments of this type are in progress [39].

If α can be measured and if continuous and discontinuous transitions can reliably be distinguished, it will then be interesting to see whether the tricritical point can be located directly. In this case, the order of the budding transition would crucially depend on the value of the parameter $\hat{m}_0$, and sufficient variations of $\hat{m}_0$ for the same vesicle (i.e., at fixed α) would lead to budding transitions of different order. Likewise a systematic investigation of the dependence of the temperature trajectories on the equilibrium area difference $\hat{m}_0$ would lead to more insight, even for the case where the budding transition is always discontinuous. This equilibrium area difference could be controlled either by using the precooling mechanism described above or by forced lipid transfer through a transmembrane pH gradient as in Ref. [9]. In such a study one could use the temperature change necessary to induce budding and the size of the vesiculated bud as important indicators to locate trajectories on a phase diagram like Fig. 3. One could then test the prediction that, the more lipid molecules are transferred to the outer layer, the smaller is the increase in temperature necessary to create budding and the smaller is the radius of the vesiculated bud. We hope that this kind of study may be possible in the not-too-distant future.

ACKNOWLEDGMENTS

APPENDIX A: THE NONLOCAL BENDING ENERGY

In this appendix, we sketch a derivation [17] from first principles of the Hamiltonian for the ADE model (4). This exercise makes explicit the origin and magnitude of the various terms, and it will allow us to estimate the ratio α of the two bending rigidities.

Consider first one monolayer leaf of the full bilayer (fluid) membrane. We may imagine this leaf to be stratified into a "head" region (h) and a "tail" or "chain" region (c). The head and chain regions have (as a consequence of all the intermolecular interactions [43]) preferred (relaxed) areas per lipid molecule $a_{h,0}$ and $a_{c,0}$, respectively, which are not in general the same. In the monolayer, the actual head and chain areas per molecule, a_h and a_c, will differ from these preferred values. We shall assume as our starting point that the elastic energy per molecule associated with this difference is

$$f(a_h,a_c) = \tfrac{1}{2}K_h a_{h,0}(a_h/a_{h,0}-1)^2 + \tfrac{1}{2}K_c a_{c,0}(a_c/a_{c,0}-1)^2 ,$$

(A1)

where K_h and K_c are area-stretching elasticities (or area-compressibility moduli) for the corresponding regions of the monolayer. In writing Eq. (A1), we picture the action of the forces in the two regions as being separately localized in two ideal surfaces separated by a distance δ. If the monolayer were planar, then a_h and a_c would be equal. When the monolayer is bent, this equality no longer holds and, as we shall see below, it is the nonzero value of the separation which is responsible for both the spontaneous curvature and the bending moduli of the monolayer. The dimensionless quantities, $(a_h/a_{h,0}-1)$ and $(a_c/a_{c,0}-1)$, are the local elastic strains associated with dilation or compression of the separate strata of the monolayer, while $K_h(a_h/a_{h,0}-1)$ and $K_c(a_c/a_{c,0}-1)$ are the associated stresses. Note that both the stresses and the strains are isotropic, as befits the fluid state of the membrane.

Since the radius of curvature of the membrane is typically large on the scale of δ, it is useful to define a suitable reference surface to describe the macroscopic shape of the (monolayer) membrane. The area per molecule a referred to this surface must be the same for heads and tails. It follows from geometry that

$$a_h = a[1+\delta_h(C_1+C_2)+\delta_h^2 C_1 C_2 + O((\delta_h C)^3)] ,$$
$$a_c = a[1-\delta_c(C_1+C_2)+\delta_c^2 C_1 C_2 + O((\delta_c C)^3)] ,$$

(A2)

where C_1 and C_2 are the local radii of curvature and δ_h and δ_c $(\delta=\delta_h+\delta_c)$ are the distances from the reference surface to the ideal head and chain surfaces, respectively.

By introducing Eq. (A2) into the elastic energy (A1), we eliminate a_h and a_c in favor of a. In doing this, it is convenient to choose δ_h and δ_c so that

$$\frac{K_h \delta_h}{a_{h,0}} - \frac{K_c \delta_c}{a_{c,0}} = 0 ,$$

(A3)

which selects as the reference surface the so-called neutral surface [44]. With this choice, we arrive at the following expression for the energy per molecule correct to quadratic order in the small quantities, (a/a_0-1) and (δC):

$$f(a,C_1,C_2)$$
$$= f_0 + a_0 \left\{ \frac{K}{2}\left[\frac{a}{a_0}-1\right]^2 + \frac{\kappa}{2}[(C_1+C_2)-C_0]^2 \right.$$
$$\left. -\kappa C_0\left[\frac{a}{a_0}-1\right](C_1+C_2)+\kappa_g C_1 C_2 \right\} ,$$

(A4)

where the parameters are given by

$$a_0 \equiv \frac{(K_h+K_c)a_{h,0}a_{c,0}}{K_h a_{c,0}+K_c a_{h,0}} ,$$

(A5)

$$K \equiv K_h + K_c ,$$

(A6)

$$\kappa \equiv \frac{K_h K_c(K_h+K_c)a_{h,0}a_{c,0}}{(K_h a_{c,0}+K_c a_{h,0})^2}\delta^2 ,$$

(A7)

$$C_0 \equiv \frac{1}{\delta}\frac{(a_{h,0}-a_{c,0})(K_h a_{c,0}+K_c a_{h,0})}{(K_h+K_c)a_{h,0}a_{c,0}} ,$$

(A8)

and

$$\kappa_g \equiv \frac{K_h K_c(K_h a_{c,0}-K_c a_{h,0})(a_{h,0}-a_{c,0})}{(K_h a_{c,0}+K_c a_{h,0})^2}\delta^2 .$$

(A9)

The monolayer energy (A4) involves both stretching (a) and bending $(C_1$ and $C_2)$ degrees of freedom. When the membrane is in its unstretched ("flaccid") state, then $|(a-a_0)/a_0| \ll 1$. If, furthermore, all local radii of curvature are large on the scale of δ, then $|\delta C_{1,2}| \ll 1$. Under these conditions the form of Eq. (A4) is that of a local Landau functional containing terms through second order in these small quantities in the most general possible way consistent with isotropy and fluidity of the membrane and a shape dependence which observes Euclidean invariance. At mechanical equilibrium, the energy (A4) is a minimum, subject to any given constraints on the number of lipid molecules $(N=\int dA/a)$ and the enclosed volume (which only involves the shape degrees of freedom). We shall assume in what follows that the lipid is insoluble, so N may be fixed by a Lagrange multiplier μ. Thus the condition for equilibrium is

$$\frac{\delta}{\delta a}\int dA \left[\frac{f(a,C_1,C_2)-\mu}{a}\right]=0 ,$$

(A10)

which leads to the relation

$$K\left[\frac{a}{a_0}-1\right]=\kappa C_0(C_1+C_2)+\frac{[f(a,C_1,C_2)-\mu]}{a_0}$$
$$\times\left[1-\frac{a-a_0}{a_0}+\cdots\right] .$$

(A11)

There is a cancellation on the right-hand side of Eq. (A11) which assures that the term linear in (C_1+C_2) disappears, so the lipid density is uniform over the neutral surface up to terms of order $(\delta/R)^2$, where R sets the scale of the vesicle size. Thus, under the conditions outlined above, the cross term in Eq. (A4) may be regarded as a small density-dependent correction to C_0 (omitted henceforth), and the elastic energy of the monolayer may finally be written,

$$f(A,C_1,C_2)=f_0+a_0\left\{\frac{K}{2}(A/A_0-1)^2\right.$$

$$\left.+\frac{\kappa}{2}[(C_1+C_2)-C_0]^2\right\}, \quad (A12)$$

where A is the actual area of the neutral surface and $A_0=Na_0$ is the preferred area of N lipid molecules.

Important conclusions already follow from Eqs. (A5)–(A9) for the monolayer parameters. We may anticipate, for example, that $a_{h,0}\sim a_{c,0}\lesssim\delta^2$ and $K_h\sim K_c$, so $C_0\lesssim 1/\delta$ and $\kappa\sim K\delta^2\sim|\kappa_g|>0$. Thus, for the typical phospholipids of Table I, we can estimate $K_h\sim K_c\sim K/2\sim 100$ ergs/cm^2 and $\delta\sim 20$ Å, so $\kappa\sim 2\times 10^{-12}$ erg, which is of the correct order of magnitude.

We turn now from the energetics of the monolayer to that of the full bilayer vesicle. We take the point of view that the bilayer is composed of two adjacent monolayers (labeled by $i=$in,out) constrained to lie at a fixed separation D (perpendicular distance between the monolayer neutral surfaces) [45]. The total elastic energy of the bilayer is

$$W\equiv\oint_{A^{\text{out}}}\frac{dA^{\text{out}}}{a^{\text{out}}}f^{\text{out}}+\oint_{A^{\text{in}}}\frac{dA^{\text{in}}}{a^{\text{in}}}f^{\text{in}}, \quad (A13)$$

where each monolayer has the energy density, $f^i=f^i(A^i,C_1^i,C_2^i)$ given by Eq. (A12), and the variables A^i, C_1^i, and C_2^i refer to the area and shape of the separate neutral surfaces of the monolayers. We now refer these quantities to a single intermediate reference surface for the bilayer whose position is a distance d^{out} inside A^{out} and d^{in} outside A^{in} ($D=d^{\text{out}}+d^{\text{in}}$). Geometry then relates the areas A^i and curvatures $C_{1,2}^i$ of the individual monolayers to those of the (new) reference surface,

$$A^{\text{out}}=A+d^{\text{out}}\oint dA(C_1+C_2)+(d^{\text{out}})^2\oint dA(C_1C_2),$$
$$A^{\text{in}}=A-d^{\text{in}}\oint dA(C_1+C_2)+(d^{\text{in}})^2\oint dA(C_1C_2), \quad (A14)$$

and

$$C_1^{\text{out}}+C_2^{\text{out}}=(C_1+C_2)-d^{\text{out}}(C_1^2+C_2^2),$$
$$C_1^{\text{in}}+C_2^{\text{in}}=(C_1+C_2)+d^{\text{in}}(C_1^2+C_2^2). \quad (A15)$$

We now substitute Eqs. (A14) and (A15) into Eq. (A13) to obtain the elastic energy functional for the full bilayer vesicle. It is again [cf. Eq. (A3)] convenient to choose for reference the bilayer neutral surface,

$$\frac{K^{\text{out}}d^{\text{out}}}{A_0^{\text{out}}}-\frac{K^{\text{in}}d^{\text{in}}}{A_0^{\text{in}}}=0. \quad (A16)$$

With this choice, the elastic energy functional for the bilayer reads

$$W=\text{const}+\frac{(K^{\text{out}}+K^{\text{in}})A_0}{2}(A/A_0-1)^2$$

$$+\frac{\kappa}{2}\oint dA[(C_1+C_2-C_0)^2+O(C_{1,2}^2D/R)]$$

$$+\frac{\bar{\kappa}}{2}\left[\frac{\pi}{AD^2}(\Delta A-\Delta A_0)^2+O(D/R)\right]$$

$$+\kappa_g\oint dA[C_1C_2+O(C_{1,2}^2D/R)], \quad (A17)$$

where

$$A_0\equiv\frac{(K^{\text{out}}+K^{\text{in}})A_0^{\text{out}}A_0^{\text{in}}}{K^{\text{out}}A_0^{\text{in}}+K^{\text{in}}A_0^{\text{out}}}, \quad (A18)$$

$$\kappa\equiv\kappa^{\text{out}}+\kappa^{\text{in}}, \quad (A19)$$

$$\bar{\kappa}\equiv\frac{K^{\text{out}}K^{\text{in}}A_0}{\pi(K^{\text{out}}A_0^{\text{in}}+K^{\text{in}}A_0^{\text{out}})}D^2, \quad (A20)$$

$$C_0\equiv\frac{\kappa^{\text{out}}C_0^{\text{out}}+\kappa^{\text{in}}C_0^{\text{in}}}{\kappa^{\text{out}}+\kappa^{\text{in}}}, \quad (A21)$$

and

$$\kappa_g\equiv\kappa_g^{\text{out}}+\kappa_g^{\text{in}}$$
$$+\frac{K^{\text{out}}K^{\text{in}}(K^{\text{out}}A_0^{\text{in}}-K^{\text{in}}A_0^{\text{out}})(A_0^{\text{out}}-A_0^{\text{in}})}{(K^{\text{out}}A_0^{\text{in}}+K^{\text{in}}A_0^{\text{out}})^2}D^2. \quad (A22)$$

The first term in Eq. (A17) represents the overall stretching energy, which is small for a flaccid vesicle. The last term is a Gaussian-curvature contribution, which de-

TABLE I. Estimate of the nonlocal bending energy. The D values, corresponding to roughly two-thirds of the total bilayer thickness, are an estimate of the thickness of the hydrocarbon region, which we use to approximate the separation of the monolayer neutral surfaces.

Lipid	κ (10^{-12} erg)	K (erg/cm^2)	D (Å)	α
SOPC (15 °C)	0.90±0.06[a]	200±13[a]	28.5±1.5[b]	1.4
DMPC (29 °C)	0.56±0.06[a]	144±8[a]	23±1[c]	1.1

[a]Reference [20].
[b]There has not been specific measurement of the thickness of SOPC lipid bilayers. This value is an estimate obtained from the thickness data given for DOPC and DSPC lipid bilayers in Ref. [46].
[c]Reference [46].

pends only on vesicle topology [12]. The remaining terms give the free-energy functional of the ADE model, Eq. (4). In particular, the third term is the so-called nonlocal bending energy, which is special to the ADE model.

Let us estimate the nonlocal bending energy. We consider only the simplest case, where the liquid bilayers are completely symmetric. Then, the monolayer area stretching moduli K^i are related to the bilayer stretching modulus K (which can be measured experimentally) as

$$K^{out} = K^{in} = K/2 .$$ (A23)

The ratio of the nonlocal bending constant to the usual, local bending rigidity is

$$\alpha \equiv \frac{\bar{\kappa}}{\kappa} = \frac{KD^2}{4\pi\kappa} .$$ (A24)

In Table I, we give the measured data for K, κ, D, and the resulting estimates of α for SOPC and DMPC vesicles. For a related estimate of α see Ref. [15].

APPENDIX B: PHASE BOUNDARIES FOR REDUCED VOLUMES NEAR UNITY

In this appendix, we discuss the asymptotic behavior of the various phase boundaries [Eqs. (20) and (21)] discussed in Sec. III in the limit $v \to 1$.

Analytical calculation of the vesiculation boundary proceeds from the geometrical constraints imposed by

the limiting shape of two kissing spheres. Let $r \equiv R_1/R_2$ be the ratio of the radius of the smaller sphere (R_1) to that of the larger sphere (R_2). The reduced volume v defined in Eq. (6) can then be expressed as

$$v = \frac{1+r^3}{(1+r^2)^{3/2}} .$$ (B1)

In the limit $v \to 1$, the approach of r to zero is described by a series in powers of $(1-v)^{1/2}$,

$$r = \sqrt{\tfrac{2}{3}}(1-v)^{1/2} + \tfrac{2}{9}(1-v)$$
$$+ \sqrt{\tfrac{1}{6}\tfrac{65}{54}}(1-v)^{3/2} + O((1-v)^2) .$$ (B2)

The reduced geometric area difference $m_L(v)$ of this limiting shape is

$$m_L(v) \equiv 4\pi\Delta a = 4\pi\frac{1+r}{(1+r^2)^{1/2}}$$
$$= 4\pi + 4\pi\sqrt{2/3}(1-v)^{1/2} + O((1-v)) .$$ (B3)

In Sec. II, we established that $G'_n = 2\bar{c}_0$, where $\bar{c}_0$ is the dimensionless Lagrange multiplier coupled to the integrated mean curvature M. The Lagrange multiplier corresponding to the two-sphere limiting shape, $\bar{C}_0$, is found to be $1/R_1 + 1/R_2$ [47]. Making use of this fact, we evaluate G'_a at the vesiculation point as

$$\bar{c}_{0,L}(v) \equiv \bar{C}_{0,L}R_A = \left[\frac{1}{R_1} + \frac{1}{R_2}\right](R_1^2 + R_2^2)^{1/2} = (1+r^2)^{1/2}\left[1 + \frac{1}{r}\right] = \frac{\sqrt{3/2}}{(1-v)^{1/2}} + \frac{2}{3} - \left[\frac{1}{6}\right]^{1/2}\frac{7}{12}(1-v)^{1/2}$$
$$+ O((1-v)) .$$ (B4)

Equations (B3) and (B4) lead straightforwardly to Eq. (20).

The phase boundary D^{pear} marks the loci of the intersection points of the energy curves of the symmetric (s) and asymmetric (a) branches,

$$W_s(\alpha, v, m_{0,D}) \equiv G_s(v, m_{s,D}) + \frac{\alpha}{2}(m_{0,D} - m_{s,D})^2$$
$$= W_a(\alpha, v, m_{0,D})$$
$$\equiv G_a(v, m_{a,D}) + \frac{\alpha}{2}(m_{0,D} - m_{a,D})^2 ,$$ (B5)

where $m_{0,D}$ is related to $m_{s,D}$ and $m_{a,D}$ via the mapping (11), i.e.,

$$m_{0,D} = m_{s,D} + (1/\alpha)G'_s(v, m_{s,D})$$
$$= m_{a,D} + (1/\alpha)G'_a(v, m_{s,D}) .$$ (B6)

In principle, the loci $m_{0,D}$ of the discontinuous boundary, along with $m_{s,D}$ and $m_{a,D}$, should be exactly solved for from Eqs. (B5) and (B6). Typically, $m_{s,D} \neq m_{a,D}$. In the following, we give only the leading asymptotic behavior of D^{pear}, as found by an approximation. Observe that, as $v \to 1, m_{s,D}$ approaches 4π as [48]

$$m_{s,D} = 4\pi + (4\pi/3)(1-v) + O((1-v)^{3/2}) .$$ (B7)

Accordingly, the bending energy G is given by

$$G_s(v, m_s) = 8\pi + O(1-v) ,$$ (B8)

so

$$W_s(\alpha,v,m_{0,D})=8\pi+O(1-v)+\frac{\alpha}{2}\{m_{0,D}-4\pi[1+\tfrac{1}{3}(1-v)+O((1-v)^{3/2})]\} \ . \tag{B9}$$

We approximate the bending energy for the asymmetric branch near the discontinuous transition point by that of the two-sphere vesiculated shape,

$$W_a(\alpha,v,m_{0,D})=2\times8\pi+\frac{\alpha}{2}\{m_{0,D}-4\pi[1+\sqrt{2/3}(1-v)^{1/2}+O(1-v)]\} \ . \tag{B10}$$

Substituting these two bending energies into Eq. (B5), we arrive at the leading-order asymptotic behavior of the discontinuous transition boundary, Eq. (21).

Concerning the line M^{pro}, where the symmetric prolate ellipse develops an instability with respect to a mode breaking the mirror symmetry, it is more difficult to make a rigorous asymptotic statement; nevertheless, our belief is that, to leading order, $m_{0,M}$ also diverges like const$/(1-v)^{1/2}$. For convenience, we construct the argument within the context of the ΔA model. In the limit $v\rightarrow1$, the symmetric shape is a slightly deformed sphere, which can be well represented by the spherical harmonics $Y_{l,0}(\theta,\phi)$ with even l. On the other hand, the first perturbative mode which breaks the mirror symmetry can be described by $Y_{l,0}(\theta,\phi)$ with odd l's. For such nearly spherical shapes, the variational free energy $\Phi[S]$, defined for the ΔA model as [23]

$$\Phi(\Sigma,P,\overline{C}_0;[S])=G[S]+\Sigma A[S]+PV[S]-2\kappa\overline{C}_0M[S] \ , \tag{B11}$$

can be expressed in terms of the amplitudes $\{a_l\}$ of the spherical harmonics [22,23,49,50]. Varying Φ with respect to $\{a_l\}$ leads to algebraic equations in $\{a_l\}$, which are equivalent to the Euler shape equations. Starting from those values of Σ, P, $\overline{C}_0$ which correspond to the $l=2$ instability of the sphere [22,23,49,50] and varying these parameters continuously, we get solutions having nonzero amplitudes for the even spherical harmonics and zero amplitudes for the odd spherical harmonics. These solutions are prolate ellipses with surface area A, volume V, and integrated mean curvature M, given as

$$A=A(\Sigma,P,\overline{C}_0), \quad V=V(\Sigma,P,\overline{C}_0), \quad M=M(\Sigma,P,\overline{C}_0) \ . \tag{B12}$$

Equations (B12) can be inverted to yield

$$\Sigma=\Sigma(A,V,M), \quad P=P(A,V,M), \quad \overline{C}_0=\overline{C}_0(A,V,M) \ . \tag{B13}$$

Near the onset of the symmetry-breaking instability, the part of Φ that depends on the amplitudes of the odd-l spherical harmonics takes the form

$$\Phi(\Sigma,P,\overline{C}_0;\{a_l,l=\mathrm{odd}\})=\sum_{l_1,l_2=\mathrm{odd}}f_{l_1,l_2}(\Sigma,P,\overline{C}_0)a_{l_1}a_{l_2}$$
$$+O(a_{l_1}a_{l_2}a_{l_3}) \ . \tag{B14}$$

At the onset of the instability, the smallest eigenvalue of the matrix of coefficients, $f_{l_1,l_2}(\Sigma,P,\overline{C}_0)$, changes sign from positive to negative. A solution for the $\{a_l\}$ with nonzero values for odd l's first develops at this point. The matrix elements $f_{l_1,l_2}(\Sigma,P,\overline{C}_0)$ in Eq. (B14) contain only the scaling form [51] $(\overline{C}_0R_A)(1-v)^{1/2}$. It is reasonable to anticipate that the condition on the smallest eigenvalue at the onset of the instability will lead to an equation of the form

$$(\overline{C}_0R_A)(1-v)^{1/2}=\mathrm{const} \ . \tag{B15}$$

The Legendre transformation, $(2\overline{C}_0R_A)=\partial G_s/\partial m$, combined with the mapping (11) then implies

$$m_{0,M}\equiv m_C+\frac{1}{\alpha}G_s\sim\frac{\mathrm{const}}{\alpha(1-v)^{1/2}} \ . \tag{B16}$$

To check this conclusion, we performed a numerical analysis of the instability for reduced volumes up to $v=0.994$. The numerical data are consistent with Eq. (B16). Furthermore, the numerical data show that const$\approx2(2.8)>2(\sqrt{3/2})$, so that, in conclusion, the spinodal line M^{pro} has the same asymptotic divergence $[1/(1-v)^{1/2}]$ as the discontinuous boundary and the vesiculation boundary (as $v\rightarrow1$) but diverges faster than those two boundaries. This implies that the spinodal line extends beyond the vesiculation boundary for values of v near unity.

[1] R. Lipowsky, Nature (London) **349**, 475 (1991).

[2] E. Sackmann, H. P. Duwe, and H. Engelhardt, Faraday Discuss. Chem. Soc. **81**, 281 (1986).

[3] E. Sackmann, H. P. Duwe, K. Zeman, and A. Zilker, in *Structure and Dynamics of Nucleic Acids, Proteins and Membranes,* edited by E. Clementi and S. Chin (Plenum, New York, 1986), p. 251.

[4] E. Evans and W. Rawicz, Phys. Rev. Lett. **64**, 2094 (1990).

[5] H. P. Duwe, J. Käs, and E. Sackmann, J. Phys. (Paris) **51**, 945 (1990).

[6] K. Berndl, J. Käs, R. Lipowsky, E. Sackmann, and U. Seifert, Europhys. Lett. **13**, 659 (1990).

[7] J. Käs and E. Sackmann, Biophys. J **60**, 825 (1991).

[8] H.-G. Döbereiner, W. Rawicz, M. Wortis, and E. Evans

(unpublished).

[9] E. Farge and P. Devaux, Biophys. J **92**, 347 (1992).

[10] P. B. Canham, J. Theor. Biol. **26**, 61 (1970). Canham introduced the bending elasticity as a contribution to the vesicle energy. His form, $(\kappa/2)(C_1^2 + C_2^2)$, for the local elastic energy differs from Eq. (1) by (a) assuming zero spontaneous curvature and (b) lacking the cross term $\kappa C_1 C_2$, which is proportional to the local Gaussian curvature. The integral of the Gaussian curvature over a closed surface is a topological invariant (Gauss-Bonnet theorem), so this latter term cannot influence either the Euler shapes or their relative energies at given (spherical) topology.

[11] W. Helfrich, Z. Naturforsch. **28c**, 693 (1973).

[12] A Gaussian-curvature term is omitted here and henceforth, since we shall deal throughout with vesicles of spherical topology.

[13] M. P. Sheetz and S. J. Singer, Proc. Natl. Acad. Sci. USA **71**, 4457 (1974).

[14] E. Evans, Biophys. J. **14**, 923 (1974); **30**, 265 (1980).

[15] W. Helfrich, Z. Naturforsch. **29c**, 510 (1974).

[16] S. Svetina, A. Ottova-Lietmannová, and R. Glaser, J. Theor. Biol. **94**, 13 (1982); S. Svetina and B. Žekš, Biomed. Biochim. Acta **42**, S86 (1983); **44**, 979 (1985).

[17] S. Svetina, M. Brumen, and B. Žekš, Stud. Biophys. **110**, 177 (1985).

[18] S. Svetina and B. Žekš, Eur. Biophys. J **17**, 101 (1989).

[19] Enforcing the constraint (2) introduces a Lagrange multiplier which plays the role of a spontaneous curvature, thus any physical asymmetry of the bilayer is irrelevant in this model.

[20] E. Evans and D. Needham, J. Phys. Chem. **91**, 4219 (1987).

[21] H. J. Deuling and W. Helfrich, J. Phys. (Paris) **37**, 1335 (1976).

[22] L. Miao, B. Fourcade, M. Rao, M. Wortis, and R. K. P. Zia, Phys. Rev. A **43**, 6843 (1991).

[23] U. Seifert, K. Berndl, and R. Lipowsky, Phys. Rev. A **44**, 1182 (1991).

[24] Even more exotic shapes have been observed experimentally, such as a spherical vesicle with tetherlike protrusions or spherical vesicles with small blebs distributed nonaxisymmetrically. These shapes are not yet understood theoretically in the context of bending energy models. Indeed, it is possible that further contributions to the energy, such as higher-order-curvature terms and van der Waals attraction of the membrane, become relevant for these shapes.

[25] M. Wortis, U. Seifert, K. Berndl, B. Fourcade, L. Miao, M. Rao, and R. K. P. Zia, in *Proceedings of the Workshop on Dynamical Phenomena at Interfaces, Surfaces, and Membranes*, edited by D. Beysens, N. Boccara, and G. Forgacs (Nova, New York, 1993), pp. 221–236.

[26] W. Wiese, W. Harbich, and W. Helfrich, J. Phys. Condens. Matter **4**, 1647 (1992). Note that these authors use a definition of α which is π times our α.

[27] R. Waugh, J. Song, S. Svetina, and B. Žekš, Biophys. J **61**, 974 (1992).

[28] U. Seifert, L. Miao, H.-G. Döbereiner, and M. Wortis, in *Structure and Conformation of Amphiphilic Membranes*, edited by R. Lipowsky, D. Richter, and K. Kremer (Springer, Berlin, 1992), pp. 93–96.

[29] B. Fourcade, L. Miao, M. Rao, M. Wortis, and R. K. P. Zia, Phys. Rev. E **49**, 5276 (1994).

[30] M. A. Peterson, J. Math. Phys. **26**, 711 (1985); J. Appl.

Phys. **57**, 1739 (1985); V. Heinrich, M. Brumen, R. Heinrich, S. Svetina, and B. Žekš, J. Phys. (Paris) II **2**, 1081 (1992).

[31] Berndl and co-workers [6,23] have noted previously in the context of the ΔA model that a very small asymmetry (one part in 10^3) in the thermal expansion coefficients of the two monolayers can have a significant effect on the temperature trajectories and, hence, on the sequence of shape transformations. This remark applies equally to the ADE model. There are as yet no measurements demonstrating such asymmetry.

[32] F. A. Nezil and M. Bloom, Biophys. J **61**, 1176 (1992).

[33] M. R. Morrow, J. P. Whitehead, and D. Lu, Biophys. J **63**, 18 (1992).

[34] J. F. Nagle and D. A. Wilkinson, Biophys. J **23**, 159 (1978).

[35] Strictly speaking, a limit shape for $v < \sqrt{2}/2$ could also be a vesiculated shape involving several segments connected by microscopic necks. In this paper, we use the term vesiculation only for the limit shape of two *spheres* of different radius.

[36] S. Svetina and B. Žekš, Eur. Biophys. J **21**, 251 (1992).

[37] In recent work [53] Käs *et al.* suggest the inclusion of a third-order term of the form $\gamma(\Delta a - \Delta a_0)^3$. By choosing a coefficient $\gamma \simeq 200$, they can generate a discontinuous transition from a weak pear to a strong pear. It is hard to regard this model as a credible explanation of the observed behavior, since the authors do not provide any rationale for the large value of γ required. In fact, the estimates sketched in Appendix A would yield a value $\gamma \simeq D/R \simeq 10^{-3}$.

[38] Once the neck closes, there are strong hysteresis effects, probably connected with short-range van der Waals forces in the region of the (microscopic) neck [52,53]. Thus reproducible cycling through the transition has not yet been achieved.

[39] Hans-Günther Döbereiner (unpublished).

[40] J. Käs and H.-G. Döbereiner (private communication).

[41] Interestingly, although these fluctuations go in both "up" and "down" directions, preliminary analysis of the fluctuations indicates that they usually do not quite average to zero, so some source of a small up-down asymmetry apparently remains [39].

[42] E. Boroske, M. Elwenspoek, and W. Helfrich, Biophys. J **34**, 95 (1981).

[43] The dominant interactions include the (attractive) hydrophobic interaction, the (repulsive) hydration force between head groups, the (repulsive) chain-chain steric interaction, and (less importantly) the van der Waals interaction.

[44] E. A. Evans and R. Skalak, in *Mechanics and Thermodynamics of Biomembranes* (CRC, Boca Raton, 1980), p. 102ff. This choice of reference surface has the effect of making the coefficient of the cross term in Eq. (A4) proportional to C_0.

[45] This picture neglects the energy associated with the forces (e.g., van der Waals attraction) which hold the monolayers at separation D. If included explicitly in Eq. (A13), such forces induce local correlations between the separate monolayer densities. Correlated lateral density modes are presumably present in the dynamical spectrum of the bilayer; however, at the mean-field level it is easy to show that there is no effect on the shape mechanics, provided that the range of the forces is small on the scale of the local curvatures $C_{1,2}$.

[46] B. A. Lewis and D. M. Engelman, J. Mol. Biol. **166**, 211 (1983).

[47] This is exactly the kissing condition we found in Ref. [22], although the form is slightly different from that in Ref. [22], which is given in its dimensionless form with the normalization chosen so that $\overline{C}_0 = 1$.

[48] In Appendix E in Ref. [23], it was proved that, for a smooth and deformed sphere, the geometric area difference m has the leading terms given here.

[49] S. T. Milner and S. A. Safran, Phys. Rev. A **36**, 4371 (1987).

[50] Ou-Yang Zhong-can and W. Helfrich, Phys. Lett. **59**, 2486 (1987); **60**, 1209 (1987); Phys. Rev. A **39**, 5280 (1989).

[51] This fact can be traced back to the perturbative development of the $l = 2$ symmetric ellipse, which can be expressed in powers of the fractional excess area $\Delta^{1/2}$ (see Ref. [22]). Note that Δ is linear in $(1-v)$ to lowest order as $v \rightarrow 1$.

[52] R. Bruinsma, J. Phys. (Paris) Colloq. **51**, C7-53 (1990).

[53] J. Käs, E. Sackmann, S. Svetina, and B. Žekš, J. Phys. (Paris) II **3**, 631 (1993).

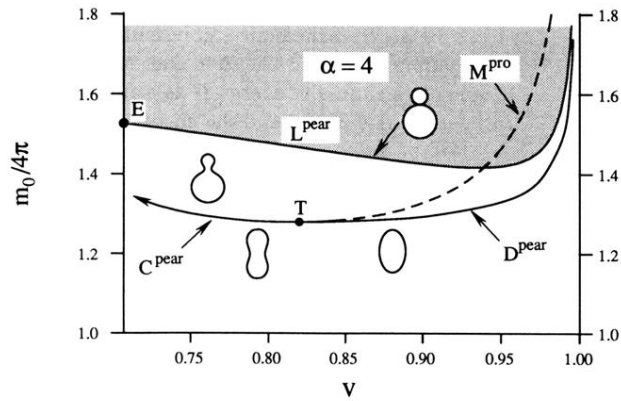FIG. 1. Phase diagram in the (v, m_0) plane involving budding and vesiculation at fixed $\alpha = 4$. Symmetric and asymmetric shapes are separated by lines of continuous transitions, C^{pear}, or discontinuous transitions, D^{pear}. These lines of budding transitions meet at the tricritical point T. The line M^{pro} denotes the limit of metastability of the symmetric shapes. The line L^{pear} denotes the vesiculation line, where the neck size has shrunk to zero. It ends at the point E, where the limiting shape consists of two spheres of equal radii. In the shaded region above this line, multiplets involving several buds become relevant (see Ref. [22]).
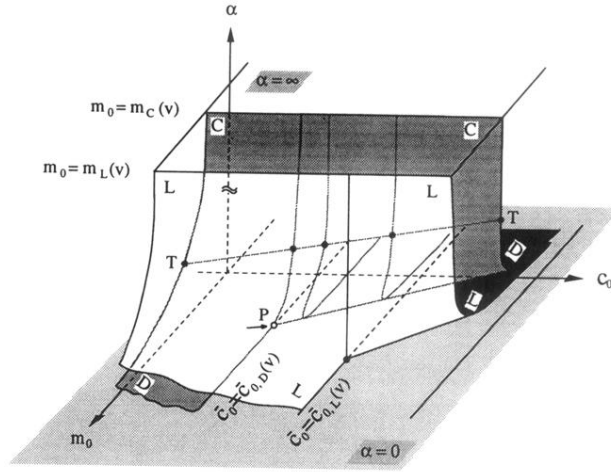
FIG. 4. Three-dimensional (α, c_0, m_0) phase diagram at a typical (constant) reduced volume. Two transition surfaces are shown. The rear (shaded) one corresponds to budding and the front (unshaded) one corresponds to vesiculation. As $\alpha \to \infty$ (one of the limiting cases), the two sheets asymptotically approach their limits, represented by the two lines $m_0(v) = m_C(v)$ and $m_0(v) = m_L(v)$, respectively. These limit lines are independent of C_0, as in the ΔA model; when $\alpha \to 0$, the discontinuous budding at $\bar{c}_{0,D}$ and the final vesiculation at $\bar{c}_{0,L}$ predicted by the SC model are asymptotically recovered. T denotes the tricritical line, which separates the continuous budding transitions, represented by the sheet C, from the discontinuous budding transitions, represented by the sheet D. The budding sheet splits along $c_{0,D} = \bar{c}_{0,D}$, and the two parts develop in opposite directions. The splitting terminates at the point P with coordinates $(\alpha = 0, c_0 = \bar{c}_{0,D}, m_0 = (m_{s,D} + m_{a,D})/2)$, where $m_{s,D}$ and $m_{a,D}$ are the actual area differences of the symmetric and asymmetric shapes at the first-order transition point in the SC model. The vesiculation sheet has a similar topology, with a splitting along the line $c_0 = \bar{c}_{0,L}$. Its splitting terminates at $(\alpha = 0, c_0 = \bar{c}_{0,L}, m_0 = m_L)$.
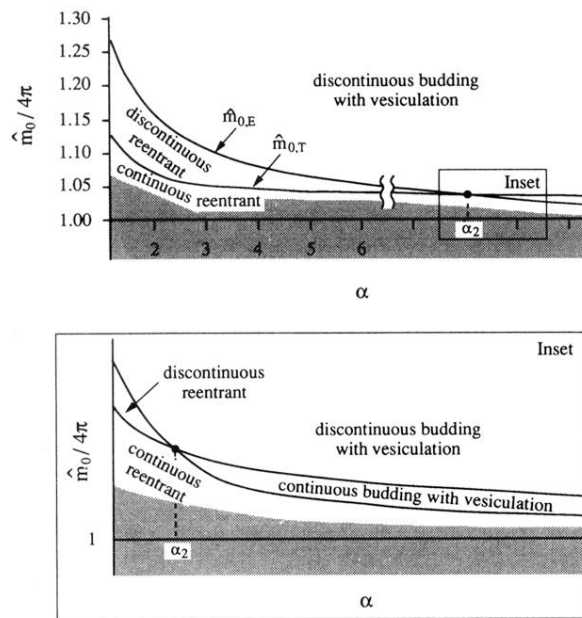
FIG. 5. Budding as a function of the equilibrium area difference $\hat{m}_0$ and α. For $\alpha > 6.5$ the curve $\hat{m}_{0,T}$ can no longer be obtained numerically. The schematic representation for large α (inset) shows the small region where continuous budding transitions with subsequent vesiculation exists. The gray area shows schematically the region in which the transition from prolates to pears is no longer present.